Reviving a failed network via microscopic interventions

Hillel Sanhedrai¹, Jianxi Gao^{2,3}, Moshe Schwartz⁴, Shlomo Havlin¹ & Baruch Barzel^{5,6,*}

- 1. Department of Physics, Bar-Ilan University, Ramat-Gan, Israel
- 2. Network Science and Technology Center, Rensselaer Polytechnic Institute, Troy, USA
- 3. Department of Computer Science, Rensselaer Polytechnic Institute (RPI), Troy, USA
- 4. Department of Physics, Tel-Aviv University, Tel-Aviv, Israel
- 5. Department of Mathematics, Bar-Ilan University, Ramat-Gan, Israel
- 6. Gonda Multidisciplinary Brain Research Center, Bar-Ilan University, Ramat-Gan, Israel
- * Correspondence: baruchbarzel@gmail.com

From mass extinction to cell death, complex networked systems often exhibit abrupt dynamic transitions between desirable and undesirable states. Such transitions are often caused by topological perturbations, such as node or link removal, or decreasing link strengths. The problem is that reversing the topological damage, namely retrieving the lost nodes/links or reinforcing the weakened interactions, does not guarantee the spontaneous recovery to the desired functional state. Indeed, many of the relevant systems exhibit a hysteresis phenomenon, remaining in the dysfunctional state, despite reconstructing their damaged topology. To address this challenge, we develop a two-step recovery scheme: first topological reconstruction to the point where the system can be revived, then dynamic interventions, to reignite the system's lost functionality. Applied to a range of nonlinear network dynamics, we identify a complex system's recoverable phase, a state in which the system can be reignited by a microscopic intervention, *i.e.* controlling just a single node. Mapping the boundaries of this newly discovered phase, we obtain guidelines for our two-step recovery.

Complex systems, biological, social or technological, often experience perturbations and disturbances, from overload failures in power systems ¹⁻⁴ to species extinction in ecological networks ⁵⁻⁷. The impact of such perturbations is often subtle, the system exhibits a minor response, but continues to sustain its global functionality ⁸⁻¹⁰. However, in extreme cases, a large enough perturbation may lead to a large-scale collapse, with the system abruptly transitioning from a functional to a dysfunctional dynamic state ¹¹⁻¹⁶. (Fig. 1a-d). For instance, in cellular dynamics, genetic knockouts, beyond a certain threshold, lead to cell death ^{17,18}; in ecological systems, changes in environmental conditions may, in extreme cases, cause mass-extinction ^{5-7,19}; and in infrastructure networks, a cascading failure, at times, results in a major blackout ^{11,20}. When such collapse occurs, the naïve instinct is to reverse the damage, retrieve the failed nodes and reconstruct the lost links. Such response however is seldom efficient, as (i) we rarely have access to all system components ²¹, limiting our ability to reconstruct the perturbed network; (ii) even if we *could* reverse the damage, due to hysteresis ²²⁻²⁴, in many cases, the system will not spontaneously regain its lost functionality ²⁵.

To address this challenge, we consider here a two-step recovery process:

Step I. Restructuring (Fig. 1e). Retrieving the network topology and weights to a point where the system *can* potentially regain its functionality.

Step II. Reigniting (Fig. 1f). Introducing dynamic interventions to steer the system back to functionality.

The challenge in Step II is that in most practical scenarios we lack direct control over the dynamic activity of the majority of the nodes. Hence we seek to reignite the system via *micro-interventions*, *i.e.* controlling just a small number of components, typically - just a single or, at most, few nodes. We, therefore, need to characterize the conditions under which such single-node reigniting can be achieved, representing the primary focus of the current contribution. Along the way, we expose a new dynamic *phase* of complex systems - the *Recoverable* phase, a state in which the system can be driven towards functionality by controlling a microscopic set of nodes.

Unlike the classic controllability challenge ^{26–32}, formulated in the context of linear dynamics, in recoverability we benefit from the nonlinear nature of the interactions. Indeed, when reigniting we do not aim to steer the system to a general arbitrary state, as done in the control theoretic setting, but rather towards one of its naturally occurring fixed-points - a problem of different nature, relying on fundamentally distinct mathematical tools ²¹.

The challenge of irreversible collapse

Consider a complex system of N components (nodes), linked through A_{ij} , a sparse, binary and random network with arbitrary degree distribution P(k). In A_{ij} the links represent dynamic interactions, whose nature depends on context. For instance, in a social system $A_{ij} = 1$ captures an acquaintance, and hence a potentially infectious interaction between individuals i and j, whereas in a sub-cellular network it may represent a regulatory interaction between gene i and gene j. To account for these dynamic distinctions we denote each node's activity by $x_i(t)$, quantifying, e.g., individual i's probability of infection or gene i's instantaneous expression level. We then track the dynamics of the system via ${}^{33-35}$

$$\frac{\mathrm{d}x_i}{\mathrm{d}t} = M_0(x_i) + w \sum_{i=1}^N A_{ij} M_1(x_i) M_2(x_j), \tag{1}$$

a general equation, characterized by three potentially nonlinear functions $M_0(x), M_1(x)$ and $M_2(x)$. The first function, $M_0(x_i)$ captures node i's self-dynamics, describing mechanisms such as protein degradation 36 (cellular), individual recovery 37,38 (epidemic) or birth/death processes 39 (population dynamics). The product $M_1(x_i)M_2(x_j)$ describes the i,j interaction mechanism, e.g., genetic activation 9,17,40 , infection 37,38 or symbiosis 41 . The mean strength of these interactions is governed by the weight w. In the context of recoverability, we seek to revive the activity of all nodes by activating a selected set of nodes, hence we focus on constructive interactions, in which nodes positively contribute to each others activity. This is expressed in Eq. (1) through $wM_1(x)M_2(x) \geq 0$ (see Supplementary Section 1). Such conditions naturally arise in many relevant applications, social, biological or ecological, as exemplified in Figs. 3a and 4a.f.

Setting the derivative on the left hand side of (1) to zero, we obtain the system's fixed-points, $\mathbf{x}_{\alpha} = (x_{\alpha,1}, \dots, x_{\alpha,N})^{\mathsf{T}}$, which, if dynamically stable, represent different *states*, desirable or undesirable, in which the system can naturally reside. Transitions between these states often result from perturbations to A_{ij} and ω , such as node/link deletion or weight change. When this occurs, it is often difficult to reverse the unwanted transition, since the system fails to spontaneously recover, even if we retrieve the lost nodes, links or the weights. To illustrate this difficulty we refer to a concrete example below.

Example 1. Cellular dynamics (Fig. 3). As our lead example we consider gene-regulation, capturing activation interactions between genes. Such genetic activation is often modeled within (1), using Michaelis-Menten dynamics ⁴⁰ (Fig. 3a). Under this framework $M_0(x_i) = -Bx_i^a$, describing degradation

(a=1), dimerization (a=2) or a more complex bio-chemical depletion process (fractional a), occurring at a rate B; below we set B=1. The activation interaction is captured by a Hill function of the form $M_1(x_i)=1$, $M_2(x_j)=x_j^h/(1+x_j^h)$, a switch-like function that saturates to $M_2(x_j)\to 1$ for large x_j , representing j's positive, albeit bounded, contribution to i's activity $x_i(t)$.

For sufficiently dense A_{ij} or large ω the system exhibits an active state \mathbf{x}_1 , in which all nodes have positive activity $(x_{1,i} > 0 \text{ for all } i)$, representing a living cell. However, perturbations to the network topology, such as link/node removal or weight reduction can cause a sharp transition to the inactive state $\mathbf{x}_0 = (0, \dots, 0)^{\top}$, in which all nodes have zero activity, i.e. cell death. To track this transition systematically we measured the average activity $\bar{x}_{\alpha} = (1/N) \sum_{i=1}^{N} x_{\alpha,i}$, which follows $\bar{x}_{\alpha} > 0$ for $\alpha = 1$ and $\bar{x}_{\alpha} = 0$ for $\alpha = 0$, as we subject it to increasing levels of topological stress: removing a q-fraction of nodes (Fig. 3b); deleting a q-fraction of links (Fig. 3d) or reducing ω by a factor q (Fig. 3c). In all cases we observe a sudden transition, as the perturbations exceed a critical threshold q_c , from $\bar{x}_{\alpha} > 0$ (green), representing the active state $\alpha = 1$, to $\bar{x}_{\alpha} = 0$ (red), representing the inactive state $\alpha = 0$.

To drive the system back to the desired \mathbf{x}_1 , the instinctive approach is to reverse the topological perturbations, namely reconstruct the deleted nodes/links or push the weight ω to its original strength. In Fig. 3f we do precisely that, finding that the system fails to recover. The reason is that while \mathbf{x}_1 is only stable above q_c , \mathbf{x}_0 is always stable - both below and above the critical point. This leads to a hysteresis phenomenon that causes the system to remain inactive, despite the reversal of the perturbation, e.g., recovering the original weight ω .

Example 1, above, while representing a specific scenario, illustrates the family of challenges that we tackle here: system's with irreversible topologically driven transitions, e.g., from a desired \mathbf{x}_1 to an undesired \mathbf{x}_0 . To revive such systems, we must dynamically reignite them by exerting external control over the activities $x_i(t)$, in order to drive them back towards the basin of attraction of \mathbf{x}_1 (Fig. 1h).

Recoverability - single-node reigniting

After restructuring A_{ij} , ω , the most natural way to reignite the system is to drive all activities x_i towards an initial condition from which the system will naturally recover to the desired \mathbf{x}_{α} . Namely, we must steer the system into \mathbf{x}_{α} 's basin of attraction (Fig. 1h)

$$\mathfrak{B}_{\alpha} = \left\{ \mathbf{x}(t=0) \mid \mathbf{x}(t\to\infty) = \mathbf{x}_{\alpha} \right\}$$
 (2)

which comprises all initial conditions $\mathbf{x}(t=0)$ from which Eq. (1) converges to $\mathbf{x}(t\to\infty)=\mathbf{x}_{\alpha}$. The problem is that such level of control over the dynamics of all nodes is seldom attainable, hence we seek to recover the system's functionality by driving just a microscopic fraction $f\to 0$ of forced nodes.

To achieve this, we consider the limit of $f \sim 1/N$, in which case our reigniting is attempted through, typically, a single, randomly selected *source* node s. To reignite the system we artificially set s's activity to $x_s(t) = \Delta > 0$, namely we externally *hold* its activity, forcing it to equal Δ . The remaining N-1 nodes continue to follow the *natural* system dynamics, *i.e.* Eq. (1), responding to the s-forcing. In technical terms, the failed state of the system, \mathbf{x}_0 , captures Eq. (1)'s initial condition, and the forced node imposes a strict boundary condition at s.

In a recoverable system, after some time, the activities will enter \mathfrak{B}_1 , at which point we can cease our external control and allow the system to naturally transition to \mathbf{x}_1 , based on its internal dynamics. This captures a successful reigniting of the system's activity. If, however, the system is non-recoverable, such single-node reigniting is insufficient, the system remains at the basin \mathfrak{B}_0 , and once we discontinue our external forcing, it relaxes back to \mathbf{x}_0 , a failed reigniting.

To analytically track the system's response to our forcing at s, we divide the rest of the network into

shells $K_s(l) = \{j \mid L_{sj} = l\}$, comprising all nodes located at distance l from s (Fig. 2a). In this notation $K_s(0) = \{s\}$, $K_s(1)$ is the group of s's nearest neighbors, $K_s(2)$ its next neighbors, and so on. Then, starting with $x_s(t) = \Delta$, we track the average activity of nodes in $K_s(l)$, via

$$x_s(l,t) = \frac{1}{|K_s(l)|} \sum_{i \in K_s(l)} x_i(t), \tag{3}$$

where $|K_s(l)|$ represents the number of nodes in $K_s(l)$. The shells adjacent to the source, *i.e.* small l, will be forced to respond to s's activation Δ , exhibiting a gain in their activity $x_s(l,t)$. However, such response may, under certain conditions, decay as l is increased, leaving the distant shells almost unaffected, and therefore still within the basin \mathfrak{B}_0 . Under these conditions, upon termination of our Δ -forcing, all shells retreat back to \mathbf{x}_0 , rendering the system unrecoverable. Successful reigniting, therefore, requires that

$$x_s(l \to \infty, t \to \infty) \in \mathfrak{B}_1,$$
 (4)

capturing a state in which the forcing at s was able to penetrate the network and impact the state of even the most distant nodes at $K_s(l \to \infty)$. This represents a recoverable system that will naturally revert to \mathbf{x}_1 once the forcing Δ is deactivated.

In Supplementary Section 2.1 we use Eq. (1) to derive a direct set of equations for the shell states $x_s(l,t)$ in (3), providing

$$\begin{cases}
 x_s(0,t) = \Delta \\
 \frac{\mathrm{d}x_s(l,t)}{\mathrm{d}t} = M_0(x_s(l,t)) + \omega M_1(x_s(l,t)) \left(M_2(x_s(l-1,t)) + \kappa M_2(x_s(l+1,t)) \right)
\end{cases}$$
(5)

a set of continuous time discrete space differential equations, with a set boundary condition at l=0, capturing our s-forcing. The functions $M_0(x), M_1(x), M_2(x)$ and the weight ω in (5) are taken from Eq. (1), and the parameter κ is extracted from A_{ij} via

$$\kappa = \frac{1}{N} \sum_{i=1}^{N} \frac{1}{k_i} \sum_{j=1}^{N} A_{ij} k_j - 1, \tag{6}$$

capturing the average neighbor's residual degree 10,42 . Starting from an initial condition, where $\mathbf{x}_s(l, t = 0) \in \mathfrak{B}_0$ for all l > 0, Eq. (5) helps us track the response of the initially failed system to our reigniting.

To extract insight from (5), we seek its steady state $x_s(l) = x_s(l, t \to \infty)$, by setting the derivatives on the left hand side to zero. We show that we can approximate this state via the recurrence relation (Supplementary Section 2.3)

$$\begin{cases} x_s(0) = \Delta, \\ F(x_s(l)) = M_2(x_s(l-1)), \end{cases}$$
(7)

where

$$F(x) = \frac{1}{\omega}R(x) - \kappa M_2 \left(R^{-1} \left(\omega M_2(x) + \omega \kappa M_2(\bar{\mathbf{x}}_0),\right)\right),\tag{8}$$

 $R(x) = -M_0(x)/M_1(x)$ and $R^{-1}(x)$ is its inverse function. The parameter $\bar{\mathbf{x}}_0$ in the right hand side of (8) represents the mean activity of nodes in $K_s(l>1)$ under the failed state \mathbf{x}_0 . Hence, we arrive at a

direct equation for the *l*-shell steady states $x_s(l)$ under any given forcing Δ .

Equations (7) and (8) represent our key result. They reduce the recoverability of (1), a multidimensional nonlinear dynamic equation, into a manageable first order recurrence relation. This recurrence takes the system's topology and weights (ω, κ) and its nonlinear dynamic mechanisms $(M_0(x), M_1(x), M_2(x))$ and hence R(x) as input, and predicts the system's recoverability as output. For any given forcing Δ , the recurrence (7) either leads to $x_s(l \to \infty) \in \mathfrak{B}_1$, satisfying the recoverability condition (4), or to $x_s(l \to \infty) \in \mathfrak{B}_0$, and hence indicating a failed recovery.

To obtain $x_s(l \to \infty)$, and observe whether it is in \mathfrak{B}_0 or \mathfrak{B}_1 , we seek the potential fixed-points of the recurrence equation (7). These points can be extracted from the solutions of

$$F(x) = M_2(x), (9)$$

capturing stationary states in which $x_s(l) = x_s(l-1)^{43,44}$. Therefore, to analyze the system's recoverability we extract the intersections of the two functions F(x) and $M_2(x)$ in (9), observing two characteristic behaviors (Fig. 2): if, for example, F(x) and $M_2(x)$ have only a single intersection $x \in \mathfrak{B}_0$, then the series inevitably converges to that point (Fig. 2c). This represents a non-recoverable system, that, regardless of the magnitude of Δ , resorts back to \mathbf{x}_0 . If, on the other hand the functions have several intersections, then its convergence depends on the boundary condition $x_s(0) = \Delta$. For $\Delta < \Delta_c$ it will approach \mathfrak{B}_0 , a failed reigniting, and for $\Delta \geq \Delta_c$ it will reach \mathfrak{B}_1 , capturing a successful reigniting (Fig. 2d,e; see also Supplementary section 2.3). Therefore, our formalism predicts both whether the system is recoverable or not, and in case it is - it predicts the required critical forcing Δ_c for reigniting. Most crucially, the patterns of intersection of (9) depend on the values of κ and ω in (8). This means that the system can transition between the recoverable and the non-recoverable phases following appropriate manipulations of ω and κ - precisely the desired guidelines for the restructuring step, which must be carried out prior to reigniting.

Next we demonstrate our framework on a range of relevant systems, starting from gene regulation (Example 1), then advancing to neuronal and ecological dynamics. We show that tracking the $l \to \infty$ limit of Eq. (7) can help us obtain direct insights into reviving collapsed systems, specifically:

- Recoverability. Given the state of the network, i.e. κ, ω , we predict whether the system can be revived by single-node reigniting or not.
- Reigniting force. In case the system is recoverable, we obtain the minimal magnitude of the forcing $\Delta \geq \Delta_c$ required for recovery.
- Restructuring. If non-recoverable, the equations offer guidelines on relevant structural interventions affecting the topology/weights, to steer ω and κ towards the recoverable phase.

Applications

Cellular dynamics (Fig. 3; see also Supplementary Section 3.1). As our first application we return to Example 1, regulatory dynamic, where $M_0(x) = -x^a$, $M_1(x) = 1$ and $M_2(x) = x^h/(1+x^h)$, and therefore $R(x) = x^a$ and $R^{-1}(x) = x^{1/a}$. Equation (9) becomes

$$\frac{1}{\omega}x^a - \frac{\kappa x^{\frac{h^2}{a}}}{x^{\frac{h^2}{a}} + \omega^{-\frac{h}{a}}(1+x^h)^{\frac{h}{a}}} = \frac{x^h}{1+x^h},\tag{10}$$

whose roots (x) determine the potential fixed points of the reignited system. Clearly, x = 0 represents a solution to (10), capturing the fact that the failed state $\mathbf{x}_0 = (0, \dots, 0)^{\top} \in \mathfrak{B}_0$ is always stable. Hence,

the question is, under what conditions do we observe a second solution x > 0, representing a potential convergence to \mathfrak{B}_1 . To answer this, we first note that while the right hand side of Eq. (10) is independent of the network topology, its left hand side, F(x), is affected by A_{ij} through κ and by its link weights through ω . Therefore, in Fig. 3f,h we plot $M_2(x)$ vs. x (yellow) and observe its intersections with F(x) (purple) as we vary the values of these two structural parameters. This allows us to observe, graphically, the potential convergence of the system to \mathfrak{B}_0 or \mathfrak{B}_1 .

First we consider $\omega = 0.8$, $\kappa = 4$ (Fig. 3g), conditions under which the system is bi-stable, and hence, in principle, can reside both in \mathbf{x}_0 or \mathbf{x}_1 . Despite this bi-stability, we find that (10) exhibits only one solution, represented by the single intersection at x = 0. This guarantees that (7) converges to $x_s(l \to \infty) = 0$, independently of Δ . Consequently, the system is non-recoverable, regardless of the strength of our forcing. The meaning is, that even though the system can potentially feature a stable \mathbf{x}_1 , it cannot be reignited from an \mathbf{x}_0 initial condition by single-node activation. Indeed, this prediction is confirmed in Fig. 3h, which indicates that the system fails to recover, despite the forcing Δ at s.

Increasing the network density to $\kappa = 7$, however, changes the picture, as now (10) features three intersection points (Fig. 3i): an unstable intermediate point (grey) and the two stable points at x = 0 (red) and at x > 0 (green), representing convergence to \mathfrak{B}_0 and \mathfrak{B}_1 , respectively. This predicts a critical forcing Δ_c (vertical grey dashed line), above which all x_i reactivate to \mathfrak{B}_1 , and below which they remain within \mathfrak{B}_0 . If $\Delta > \Delta_c$ the system will be successfully reignited by controlling just a single node, as all shells will, eventually be driven into \mathfrak{B}_1 , and then naturally converge to the desired \mathbf{x}_1 . Fig. 3j shows just that, as now the system responds to our forcing, and, as predicted, recovers its lost functionality.

The results above uncover the existence of a novel, previously overlooked, dynamic phase. Indeed, the regulatory system of Fig. 3a has been previously shown to follow two phases, *inactive*, where only \mathbf{x}_0 is stable vs. *bi-stable* where both \mathbf{x}_0 and \mathbf{x}_1 are stable, depending on initial conditions (Fig. 3b-d). Our analysis here uncovers a third phase: *recoverable*, a subspace of the bi-stable phase, in which the system can be reignited from \mathbf{x}_0 to \mathbf{x}_1 by controlling a microscopic set of nodes, here just one single node. The parameters driving this three state phase space are ω , κ and Δ , which together determine the existence (and if exists - the value) of the critical forcing required to revive the inactive system. In Fig. 3k we show these phases in the ω , κ space, as obtained from numerically simulating the states of the system for $\sim 10^3$ different combinations of ω and κ (Supplementary Section 4.3). The white solid line represents our theoretical prediction, based on analyzing the intersections of (10), indicating that the boundaries of recoverability can be well-approximated by our analytical framework. We also present the ω , Δ and κ , Δ phase diagrams, further indicating the agreement between simulation and theory (Fig. 3l,m).

To further test our predictions in an empirical setting, we collected data on two real biological networks, capturing protein interactions in Human 45 ($\kappa = 21.7$) and Yeast 46 ($\kappa = 10.7$) cells. In these networks the interaction topology A_{ij} is extracted from empirical data, but the average weight ω , determining the interaction rates can change due to environmental conditions. We, therefore set, for each network, two different weights (Fig. 3n): for Human we set $\omega_1 = 0.2$ (Human UR orange) and $\omega_2 = 1$ (Human R blue), the former in the unrecoverable phase, and the latter - recoverable. Similarly, for Yeast we set $\omega_1 = 0.4$ (Yeast UR, orange, unrecoverable) and $\omega_2 = 1$ (Yeast R, blue, recoverable). As predicted, we find in Fig. 3n,o that, indeed, Yeast UR and Human UR remain inactive under reigniting. This is while Yeast R and Human R, both predicted to reside in the recoverable phase, can be successfully revived via single-node reigniting.

Neuronal dynamics (Fig. 4a-e, Supplementary Section 3.2). As our second example we consider the Cowan-Wilson neuronal dynamics 47,48 , in which (1) follows the form shown in Fig. 4a. The system naturally exhibits three dynamic phases. The *inactive* state \mathbf{x}_0 , in which all activities are suppressed, is obtained when the network is extremely sparse, *i.e.* small κ, ω . The *active* \mathbf{x}_1 , in which x_i are relatively large, is observed when ω, κ are high. In between these two extremes the system features a *bi-stable* phase,

in which both \mathbf{x}_0 and \mathbf{x}_1 are potentially stable. In Fig. 4b,c we observe these phases on a a set of random networks with varying ω , obtaining two critical points $\omega_{c,1} < \omega_{c,2}$ (dashed grey lines), in which the system transitions between active, inactive and bi-stable. This phase-space predicts a hysteresis phenomenon: if ω is driven below $\omega_{c,1}$ and the system fails, it will not spontaneously recover unless we retrieve ω to be above $\omega_{c,2}$.

Our formalism, however, predicts an additional, previously unknown dynamic phase, in which the system is recoverable. This phase, shown in Fig. 4d (blue) represents a sub-space of the bi-stable regime, in which the failed system, if untouched, remains at \mathbf{x}_0 as per the above hysteresis. Yet, under single-node reigniting, it can be forced back towards activity (\mathbf{x}_1). To demonstrate this we collected data on the structure of a human brain network ⁴⁹ to construct A_{ij} ($\kappa = 6.6$), and simulated neuronal dynamics using $\omega_1 = 2$, in the unrecoverable phase (Brain UR, orange), and $\omega_2 = 4$, which is recoverable (Brain R, blue). Indeed, Fig. 4e confirms that Brain UR remains inactive, while Brain R's activity is successfully revived.

Mutualistic population dynamics (Fig. 4f-j, Supplementary Section 3.3). As our final example we examine symbiotic interactions in ecological networks, such as plant-pollinator relationships 50 . Once again, we find a window of recoverability, in which one can steer a collapsed system towards activity via single-node reigniting. Here we used an empirical plant-pollinator network 51 , Eco, to examine recoverability (Fig. 4i,j), a low ω unrecoverable Eco UR (orange) and an increased ω recoverable Eco R (blue).

Taken together, these examples demonstrate the predictive power of our framework, which allows to systematically map the conditions for recoverability. Next, we show how to use the obtained recoverability maps to provide direct insights into our proposed two-step recovery, extracting guidelines for reviving a collapsed network.

Restructuring guidelines

To successfully reignite a failed system we must first steer it from the non-recoverable to the recoverable phase. This can be achieved through appropriate restructuring interventions to impact ω or κ , for instance, increasing weights or adding nodes/links. The phase diagrams of Figs. 3k-m and 4d,i can provide guidelines for such restructuring, as, indeed, they indicate what interventions can potentially push us closer to the recoverable phase.

To illustrate this, in Fig. 5a-d we simulate a cellular network (Yeast) that has been driven towards inactivity due to major topological perturbations, such as node or link deletion (grey nodes/links). Some of the removed components are inaccessible (red), and hence when restructuring we cannot retrieve them. To revive the system, under these constraints, we incorporate our proposed two-step recovery:

• Step I. Restructuring. First we conduct topological interventions, to bring the system to the recoverable phase. As explained above, certain nodes or links are inaccessible to us (red), hence our potential interventions are restricted. The challenge is, therefore, to design a set of accessible interventions that will enable us to revive the system's dynamic activity. As recoverability is driven by two relevant parameters, κ and ω , we map all potential intervention to their effect on these two parameters (Fig. 5e). Indeed, a sequence of such interventions represents a path in the κ , ω space. Therefore, in the restructuring step we seek paths of accessible interventions originating in the present state of the system, and delivering the network into the bounds of the recoverable phase (Fig. 5f). Our goal, we emphasize, is not to simply retrieve the lost nodes and links, but to achieve recoverability. This designates, not a single point, but rather an entire sub-space in κ , ω (Fig. 5f, blue), affording us some level of restructuring flexibility. As a result, despite the constraints imposed by the network's irretrievable components, we are able to design three distinct restructuring paths, all originating in the current state of the failed system (Yeast perturbed, white), but leading to different destinations - Net 1,2 or 3 - within the recoverable sub-space.

• Step II. Reigniting. Once in the recoverable phase we can revive the system via single-node reigniting, and retain its lost activity, as shown in Fig. 5g for the three restructured networks Net 1.2 and 3.

This example illustrates how the phase diagrams of recoverability provide direct guidelines for restructuring. For example, in Fig. 5f path 1 builds mainly on controlling the interaction strength (ω) , but assumes little freedom to add nodes or links (κ) . In contrast path 3 involves a significant component of adding nodes/links to A_{ij} , affecting not just ω but also κ . The optimal restructuring path is, therefore, determined by the nature of our constraints, for example, the relative difficulty in adding weights as in path 1, vs. adding nodes/links, a la path 3. The crucial point is, that, knowing the phase-boundaries of recoverability, we were able to set different end-points for each path (Net 1,2,3), providing us with a spectrum of potential interventions - either focusing on ω , and hence aiming for end-point 1, or focusing on κ , and thus seeking to reach end-point 3. Such flexibility, enabled thanks to our phase-diagrams, is crucial for real-world restructuring.

While the potential space of structural interventions in Step I is incomprehensibly vast, our phase diagrams reduce this space into just two relevant control parameters - κ , characterizing A_{ij} 's density, and ω , capturing its link weights. This allows us to asses the contribution of all potential interventions by quantifying their effect on these two parameters - enabling to seek optimal pathways for crossing the recoverability phase boundary.

Interestingly, our phase diagrams indicate that κ and ω may play unbalanced roles: for example Fig. 5f shows that the phase boundary from unrecoverability to recoverability in the κ , ω space becomes almost flat in the limit of large κ (white solid line). This implies that while it may only require a small change in ω , *i.e.* pushing the system in the vertical direction, to transition a network towards recoverability, doing so through κ , along the horizontal axis, is by far more difficult. Indeed, in Supplementary Section 3.1.3 we show that in the limit of large h in Fig. 3a, the phase boundary becomes almost independent of κ , and the effect of increasing ω becomes dominant. Hence, under cellular dynamics, increasing weights, when possible, is a preferred strategy over adding links. This offers a quite general restructuring guideline, that can help design efficient κ , ω -paths in our two-step recovery scheme.

Discussion and outlook

While the structure of complex networks has been deeply investigated over the years, our understanding of their dynamics is still emerging. The challenge is often focused on *prediction*, aiming to foresee a network's dynamic behavior. Here, we go a step further, and focus on *influence*, showing how to steer a system towards a desired behavior.

At first glance, this challenge seems to be associated with network controlability. There are, however two crucial distinctions between recoverability and controlability: (i) Control theory revolves around linear dynamics, and is therefore fully characterized by the network structure/weights (A_{ij}, ω) . Recoverability, in contrast, is tailored for nonlinear systems within the form (1), hence driven by the interplay of this structure with the system's intrinsic dynamics. Indeed, the phase boundaries of recoverability strongly depend on the system's interaction mechanisms $M_0(x), M_1(x), M_2(x)$, as observed in Figs. 3k-m and 4d,i. (ii) On the other hand, while controlability aspires to drive a system between any two arbitrary states, an unsolved challenge under nonlinear dynamics, recoverability is limited to the system's naturally occurring fixed-points.

The main advantage of item (ii) above, is that it allows us to revive a failed system using an extremely simple control signal, namely the constant forcing Δ . Had we needed a more delicate fine-tuned input, our strategy would have likely been too sensitive and impractical. Fortunately in recoverability, one only needs to kick the system out of its undesired basin, then let it relax to \mathbf{x}_1 independently ²¹ (Fig. 1h).

Such crude level of control, we find, is possible even under the rather broad conditions captured by Eq. (1).

The microscopic behavior of complex networks is driven by countless parameters, from the fine-structure of A_{ij} to the specific rates of each node's dynamic processes. Our analysis, however, shows, that their large-scale functionality can be traced to a manageable set of relevant parameters, e.g., κ, ω and Δ . Such dimension reduction is the fundamental premise of statistical physics, allowing to analyze systems with endless degrees of freedom using a limited set of statistical entries. We believe, that a similar approach to network dynamics, can help us understand, predict, and ultimately influence the behavior of complex multi-dimensional systems.

References

- [1] G. Caldarelli. Scale-free networks: complex webs in nature and technology. Oxfrod University Press, New York, 2007.
- [2] P. Van Mieghem. Graph Spectra for Complex Networks. Cambridge University Press, Cambridge, UK, 2010.
- [3] J. Zhao, D. Li, H. Sanhedrai, R. Cohen and S. Havlin. Spatio-temporal propagation of cascading overload failures in spatially embedded networks. *Nature Communications*, 7:10094 99, 2016.
- [4] I. Dobson, B.A. Carreras, V.E. Lynch and D.E. Newman. Complex systems analysis of series of blackouts: Cascading failure, critical points, and self-organization. *Chaos*, 17:026103, 2007.
- [5] H.-Y. Shih, T.-L. Hsieh and N. Goldenfeld. Ecological collapse and the emergence of travelling waves at the onset of shear turbulence. *Nature Physics*, 12(3):245–248, 2016.
- [6] J. Jiang, A. Hastings and Y.-C. Lai. Harnessing tipping points in complex ecological networks. *Journal of the Royal Society Interface*, 16(158):20190345, 2019.
- [7] R.M. May. Thresholds and breakpoints in ecosystems with a multiplicity of stable states. Nature, 269:471–477, 1977.
- [8] R. Cohen, K. Erez, D. Ben-Avraham and S. Havlin. Breakdown of the internet under intentional attack. Physical Review Letters, 86(16):3682, 2001.
- [9] H.I. Schreier, Y. Soen and N. Brenner. Exploratory adaptation in large random networks. *Nature Communications*, 8(1):1–9, 2017.
- [10] J. Gao, B. Barzel and A.-L. Barabási. Universal resilience patterns in complex networks. Nature, 530:307—-312, 2016.
- [11] S.V. Buldyrev, R. Parshani, G. Paul, H.E. Stanley and S. Havlin. Catastrophic cascade of failures in interdependent networks. *Nature*, 464:1025–1028, 2010.
- [12] P. Van Mieghem. Performance analysis of complex networks and systems. Cambridge University Press, 2014.
- [13] A.E. Motter and Y.-C. Lai. Cascade-based attacks on complex networks. Physical Review E, 66:065102, 2002.
- [14] P. Crucitti, V. Latora and M. Marchiori. Model for cascading failures in complex networks. Physical Review E, 69:045104–7, 2004.
- [15] D. Achlioptas, R.M. D'Souza and J. Spencer. Explosive percolation in random networks. Science, 323:1453–1455, 2009.
- [16] S. Boccaletti, J.A. Almendral, S. Guana, I. Leyvad, Z. Liua, I.S. Nadal, Z. Wang and Y. Zou. Explosive transitions in complex networks' structure and dynamics: Percolation and synchronization. *Physics Reports*, 660:1–94, 2016.
- [17] U. Alon. An Introduction to Systems Biology: Design Principles of Biological Circuits. Chapman & Hall, London, U.K., 2006.
- [18] H. Jeong, S.P. Mason, A.-L. Barabási and Z.N. Oltvai. Lethality and centrality in protein networks. *Nature*, 411:41, 2001.
- [19] F. Courchamp, E. Angulo, P. Rivalan, R.J. Hall, L. Signoret, L. Bull and Y. Meinard. Rarity value and species extinction: the anthropogenic allee effect. *PLoS Biol*, 4(12):e415, 2006.
- [20] A.M. Lyapunov. The general problem of the stability of motion. International Journal of Control, 55:531–534, 1992.
- [21] S.P. Cornelius, W.L. Kath and A.E. Motter. Realistic control of network dynamics. *Nature Communications*, 4:1942–1950, 2013.
- [22] H. Behar, N. Brenner, G. Ariel and Y. Louzoun. Fluctuations-induced coexistence in public goods dynamics. Physical Biology, 13(5):056006, 2016.
- [23] X. Zhang, S. Boccaletti, S. Guan and Z. Liu. Explosive synchronization in adaptive and multilayer networks. Physical Review Letters, 114(3):038701, 2015.
- [24] G. Zeng, J. Gao, L. Shekhtman, S. Guo, W. Lv, J. Wu, H. Liu, O. Levy, D. Li, Z. Gao, H.E. Stanley and S. Havlin. Multiple metastable network states in urban traffic. *Proceedings of the National Academy of Sciences*, 117(30):17528–17534, 2020.

- [25] Antonio Majdandzic, Boris Podobnik, Sergey V Buldyrev, Dror Y Kenett, Shlomo Havlin, and H Eugene Stanley. Spontaneous recovery in dynamical networks. *Nature Physics*, 10(1):34–38, 2014.
- [26] G. Yan, G. Tsekenis, B. Barzel, J.-J. Slotine, Y.-Y. Liu and A.-L. Barabási. Spectrum of controlling and observing complex networks. *Nature Physics*, 11:779–786, 2015.
- [27] Y.-Y. Liu, J.-J. Slotine and A.-L. Barabási. Controllability of complex networks. Nature, 473:167–173, 2010.
- [28] F. Sorrentino, M. Di Bernardo, F. Garofalo and G. Chen. Controllability of complex networks via pinning. Physical Review E, 75(4):046103, 2007.
- [29] Z. Yuan, C. Zhao, Z. Di, W.-X. Wang and Y.-C. Lai. Exact controllability of complex networks. Nature Communications, 4(1):1–9, 2013.
- [30] T. Nepusz and T. Vicsek. Controlling edge dynamics in complex networks. Nature Physics, 8(7):568–573, 2012
- [31] A. Chiuso, L. Fortuna, M. Frasca, A. Rizzo, L. Schenato and S. Zampieri. Modelling, Estimation and Control of Networked Complex Systems. Springer, 2009.
- [32] L. Fortuna, S. Graziani, A. Rizzo and M.G. Xibilia. Soft sensors for monitoring and control of industrial processes. Springer Science & Business Media, 2007.
- [33] B. Barzel and A.-L. Barabási. Network link prediction by global silencing of indirect correlations. Nature Biotechnology, 31:720 – 725, 2013.
- [34] U. Harush and B. Barzel. Dynamic patterns of information flow in complex networks. Nature Communications, 8:2181, 2017.
- [35] C. Hens, U. Harush, R. Cohen, S. Haber and B. Barzel . Spatiotemporal propagation of signals in complex networks. *Nature Physics*, 15:403, 2019.
- [36] B. Barzel and O. Biham. Binomial moment equations for stochastic reaction systems. Physical Review Letters, 106:150602-5, 2011.
- [37] P.S. Dodds and D.J. Watts. A generalized model of social and biological contagion. *Journal of Theoretical Biology*, 232:587–604, 2005.
- [38] R. Pastor-Satorras, C. Castellano, P. Van Mieghem and A. Vespignani. Epidemic processes in complex networks. Rev. Mod. Phys., 87:925–958, 2015.
- [39] T.S. Gardner, C.R. Cantor and J.J. Collins. Construction of a genetic toggle switch in escherichia coli. Nature, 403:339, 2000.
- [40] G. Karlebach and R. Shamir. Modelling and analysis of gene regulatory networks. *Nature Reviews*, 9:770–780, 2008
- [41] C.S. Holling. Some characteristics of simple types of predation and parasitism. The Canadian Entomologist, 91:385–398, 1959.
- [42] M.E.J. Newman. Networks an introduction. Oxford University Press, New York, 2010.
- [43] R.M. May. Simple mathematical models with very complicated dynamics. Nature, 261:459-467, 1976.
- [44] S.H. Strogatz. Nonlinear dynamics and chaos with student solutions manual: With applications to physics, biology, chemistry, and engineering. CRC press, 2018.
- [45] J.F. Rual et al. Towards a proteome-scale map of the human protein-protein interaction network. Nature, 437:1173-1178, 2005.
- [46] H. Yu et al. High-quality binary protein interaction map of the yeast interactome network. Science, 322:104–110, 2008.
- [47] H.R. Wilson and J.D. Cowan. Excitatory and inhibitory interactions in localized populations of model neurons. *Biophysical Journal*, 12(1):1–24, 1972.
- [48] H.R. Wilson and J.D. Cowan. A mathematical theory of the functional dynamics of cortical and thalamic nervous tissue. *Kybernetik*, 13(2):55–80, 1973.
- [49] E. Bullmore and O. Sporns. Complex brain networks: graph theoretical analysis of structural and functional systems. *Nature reviews neuroscience*, 10(3):186–198, 2009.
- [50] J.N. Holland, D.L. DeAngelis and J.L. Bronstein. Population dynamics and mutualism: functional responses of benefits and costs. American Naturalist, 159:231–244, 2002.
- [51] Interaction web database. http://www.nceas.ucsb.edu/interactionweb/resources.

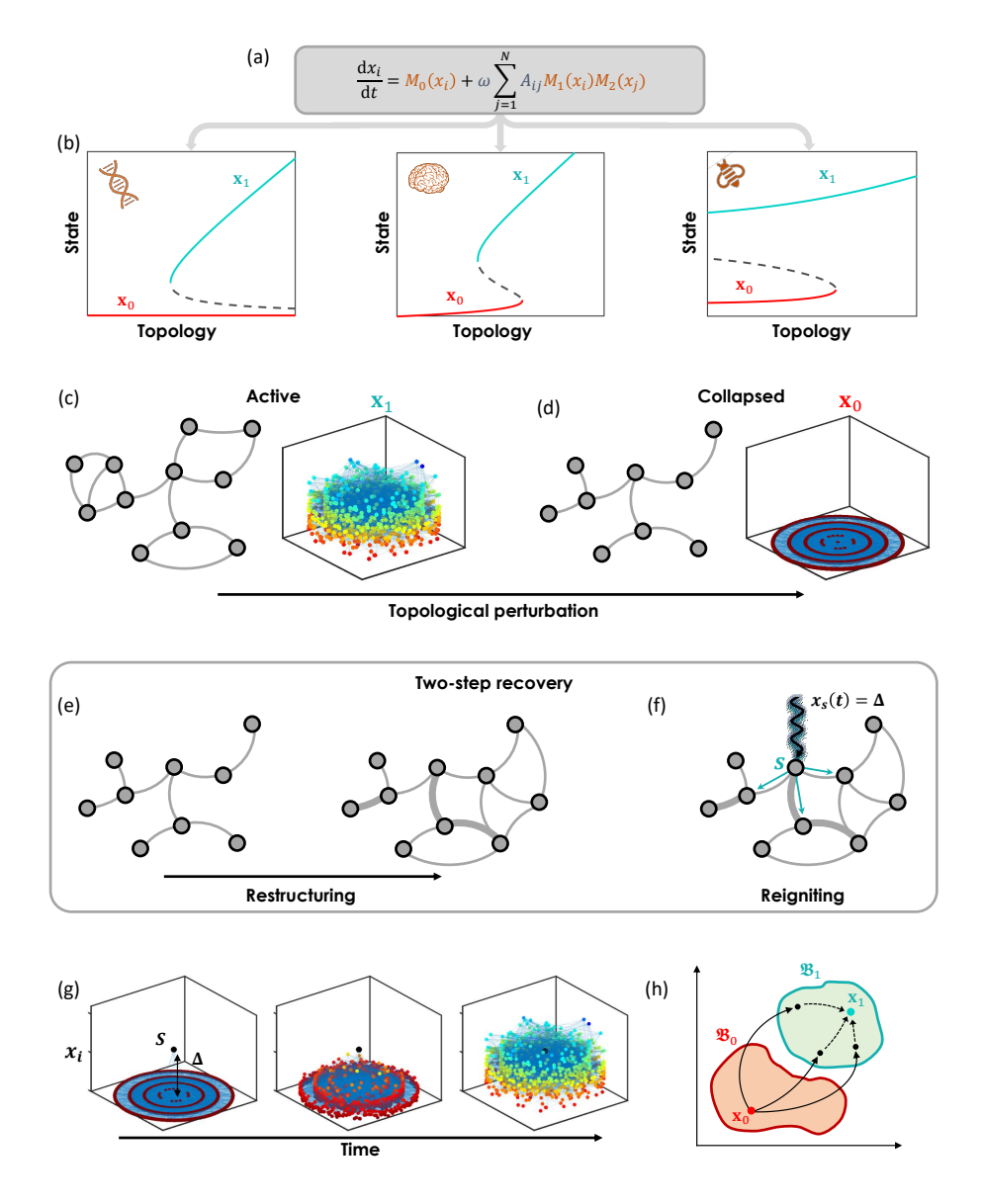


Figure 1: Reviving a failed network. (a) The components of our modeling framework: The network topology is captured by the adjacency matrix A_{ij} and the link weights ω (grey terms); the interaction mechanisms, i.e. the dynamics, are captured by the nonlinear functions $M_0(x), M_1(x), M_2(x)$ (orange terms). (b) Depending on the dynamics - e.g., cellular, neuronal or ecological - the system exhibits distinct fixed-points, active (\mathbf{x}_1 , green) or failed $(\mathbf{x}_0, \text{ red})$; intermediate unstable points are marked by grey dashed lines. The transitions between these states are driven by perturbations to the topology (A_{ij}, ω) . (c) Under the unperturbed topology the system resides in the functional state \mathbf{x}_1 , in which all nodes are active, i.e. $x_i > 0$. In this presentation, which we also use throughout the paper, the network nodes are laid out on the x, y plane, and their activities x_i are captured by the z coordinate. Hence, an active system has all nodes spread out along the positive z-axis, while a failed network is laid out around z=0. We also use color coding from red (small x_i) to blue (large x_i) as visual aid. (d) Perturbations to the topology, such as node/link removal or weight reduction, result in a collapse to the inactive \mathbf{x}_0 , here having all activities vanish (z=0). (e) **Restructuring**. To revive the failed system we must first restructure its topology to a point where it can recover, namely a point where \mathbf{x}_1 is potentially stable. This, however, is insufficient, as often the system will not spontaneously retain its lost activity. (f) Reigniting. After restructuring we reignite the active state \mathbf{x}_1 by controlling a microscopic set of nodes, here the single node s. The controlled node is forced to sustain a constant activity $x_s(t) = \Delta$. This activating force then spreads to impact all other nodes in the network and push them towards \mathbf{x}_1 . (g) The state of the network in three different time-points following single-node reigniting, forcing $x_s(t) = \Delta$ (black node at center). The reigniting force gradually impacts the network, until the system's activity \mathbf{x}_1 is restored. (h) In this process we use the natural basin structure of our dynamics. The basin \mathfrak{B}_{α} captures all initial states, from which the system (1) converges to the fixed-point \mathbf{x}_{α} . Therefore, to reignite \mathbf{x}_1 we seek to steer the system from \mathfrak{B}_0 (red) to any point within \mathfrak{B}_1 (green). Once in \mathfrak{B}_1 , we can cease our forcing, and the system will spontaneously transition to the desired \mathbf{x}_1 (dashed arrows).

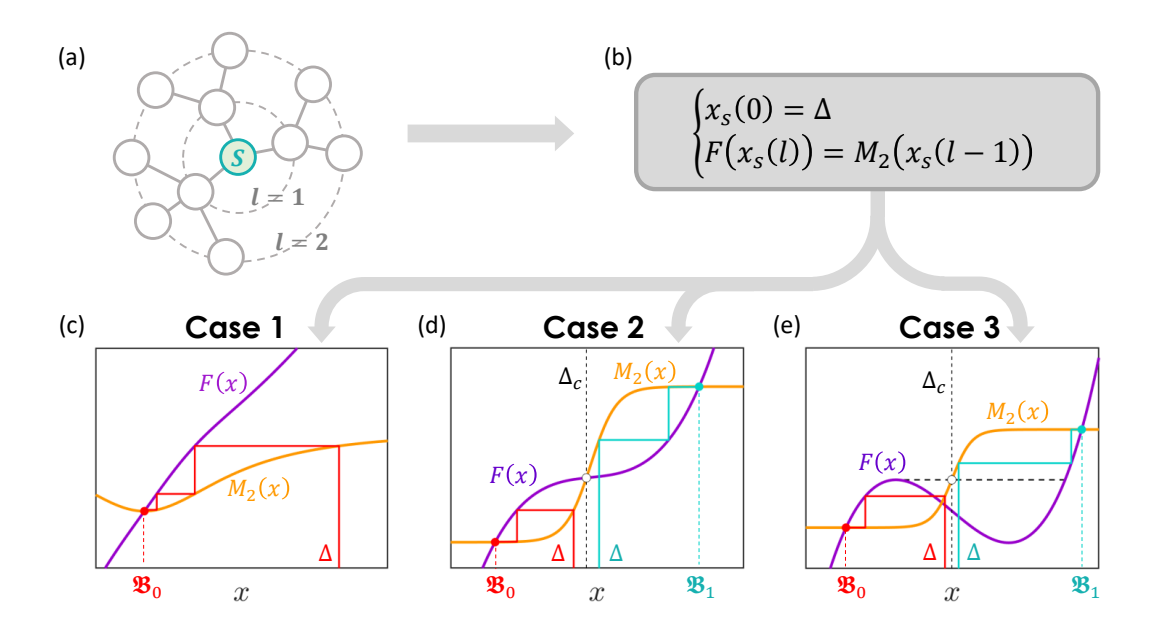


Figure 2: Can a system be reignited by a single node? (a) During reigniting we select a single source node s and, for a limited time, we artificially force it to sustain a permanent activity Δ . To track the system's response to such forcing, we divide the network into shells $K_s(l)$ comprising all nodes at distance l from s. (b) The reignited activity $x_s(l)$ of all nodes at $K_s(l)$ is tracked via the recurrence relation of Eq. (7), starting from our forcing at s (top equation), and tracking its propagation as it penetrates the network shells (bottom equation). Successful reigniting requires $x_s(l \to \infty) \in \mathfrak{B}_1$, i.e. that the distant shells were driven towards the desired basin. (c) - (e) We can track the convergence of the recurrence relation graphically by plotting F(x) (purple) and $M_2(x)$ (yellow). The forcing Δ determines our initial starting point, and the recurrence can be tracked via the red or green trajectories. The final state $x_s(l \to \infty)$ is reached when the two functions, F(x) and $M_2(x)$, intersect. We observe three potential scenarios (Supplementary Section 2.3): Case 1. F(x) and $M_2(x)$ have a single intersection point in \mathfrak{B}_0 (red). Under these conditions, regardless of the initial value (Δ) the recurrence converges to $\mathbf{x}_s(l\to\infty)\in\mathfrak{B}_0$, and hence the system is unrecoverable. Case 2. F(x) and $M_2(x)$ exhibit two intersections, corresponding to the system's two stable fixed points \mathbf{x}_0 (red) and x_1 (green); the intermediate intersection (grey) is unstable. Here, for $\Delta < \Delta_c$ the system converges to \mathfrak{B}_0 , i.e. unrecoverable (red trajectory), while for $\Delta \geq \Delta_c$ it approaches \mathfrak{B}_1 - hence it is recoverable (green trajectory). Case 3. In case F(x) is non-monotonic the critical forcing Δ_c is determined by F(x)'s local maximum point (grey dashed lines), see Supplementary Section 2.3 for a detailed analysis of Case 3.

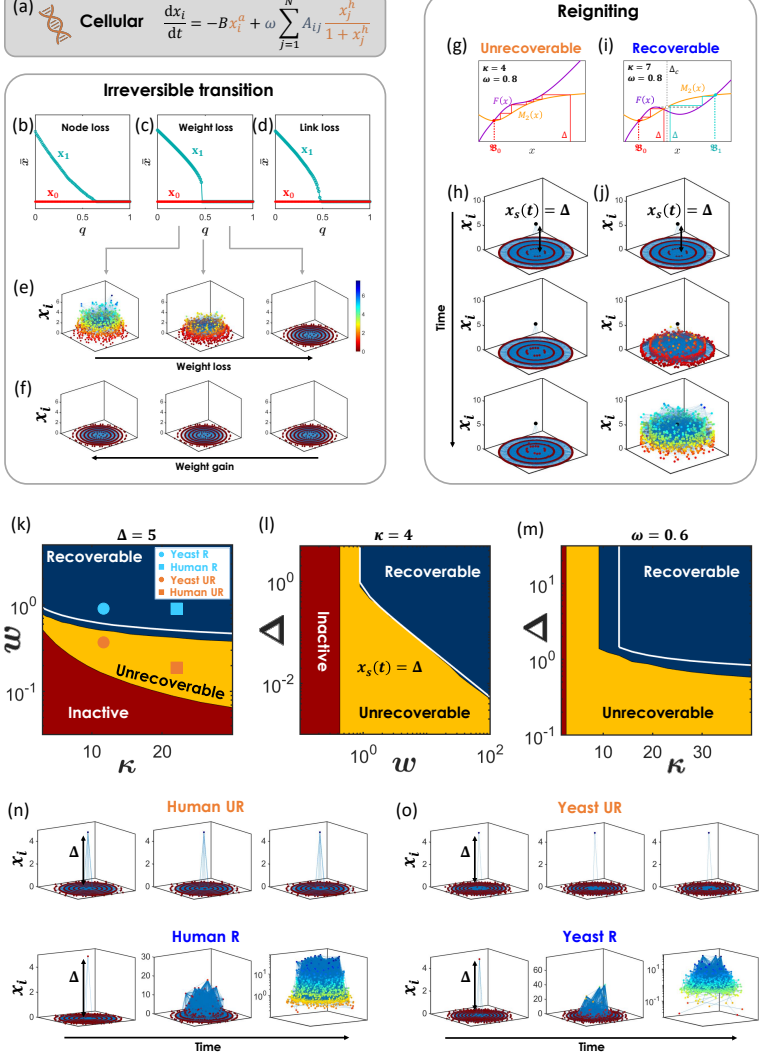


Figure 3: Recoverability of cellular dynamics. (a) Gene regulation as modeled via the Michaelis-Menten dynamics. (b) - (d) The average steady-state activity \bar{x} as obtained from cellular dynamics following topological perturbation: deletion of a q-fraction of nodes; factor q reduction of weights and removal of a q-fraction of links. While the active \mathbf{x}_1 is only stable for $q < q_c$ (green), the inactive \mathbf{x}_0 is always stable (red). Hence the system undergoes an irreversible collapse at $q = q_c$. (e) We track three specific states, capturing the steady-state activities x_i under varying levels of weight loss q. When q is small (left) all x_i are positive and the system is in the active state \mathbf{x}_1 . x_i gradually decline as q increases (center), until the system collapses into the inactive state \mathbf{x}_0 , in which all x_i vanish (right). (f) Reversing the perturbation does not revive the system. Here we retrieve the lost weights, however, since \mathbf{x}_0 is always stable, the system remains in the collapsed state, avoiding spontaneous recovery. To revive the failed system we apply single-node reigniting: (g) The functions F(x) (purple) and $M_2(x)$ (yellow) as obtained from the left/right hand sides of Eq. (10), setting $\kappa = 4, \omega = 0.8$. The system follows Case 1 of Fig. 2c, exhibiting a single intersection $(\mathfrak{B}_0, \text{ red})$, and hence it is unrecoverable. (h) Indeed, forcing node s to a permanent Δ activity (black node), the remaining shells fail to reignite. (i) Under a denser A_{ij} with $\kappa = 7$ the function F(x) takes a different form and the system now follows Case 3. It is now recoverable if the forcing $\Delta \geq \Delta_c = 0.9$ (vertical dashed line). (j) As predicted, now the system is successfully activated via single-node reigniting. (k) The phase diagram in the κ, ω plane (Supplementary Section 4.3). We observe the three predicted phases: inactive (red), where only \mathbf{x}_0 is stable, unrecoverable (yellow), where \mathbf{x}_1 is potentially stable, but unattainable via single-node reigniting, and recoverable (blue), where the system can be revived by a single node. The theoretical prediction obtained from the roots of Eq. (10) is also shown (white solid line). (1) The phase diagram in the ω, Δ space. Here, for $\omega < 0.9$ the system is never recoverable. Above that, the higher is ω the smaller is the forcing Δ required for reigniting. Our theoretical prediction is also shown (white solid line). (m) The κ, Δ phase diagram. The slight discrepancy between theory (white solid line) and simulation (yellow-blue transition) is likely due to the discrete nature of κ . (n) To examine our prediction in an empirical setting we used the human protein interaction network 45 ($\kappa = 21.7$) to construct A_{ij} under two values of ω : Human UR with $\omega = 0.2$, in the unrecoverable phase, and Human R, with $\omega = 1$, which is recoverable (see panel k, orange vs. blue squares). Indeed, while Human UR cannot be revived (top), Human R is successfully reignited by a single node (bottom). (o) Similar results are observed also for the Yeast network 46 ($\kappa = 10.7$, orange vs. blue circles in panel k) under $\omega = 0.4$ (Yeast UR, unrecoverable) and $\omega = 1$ (Yeast R, recoverable).

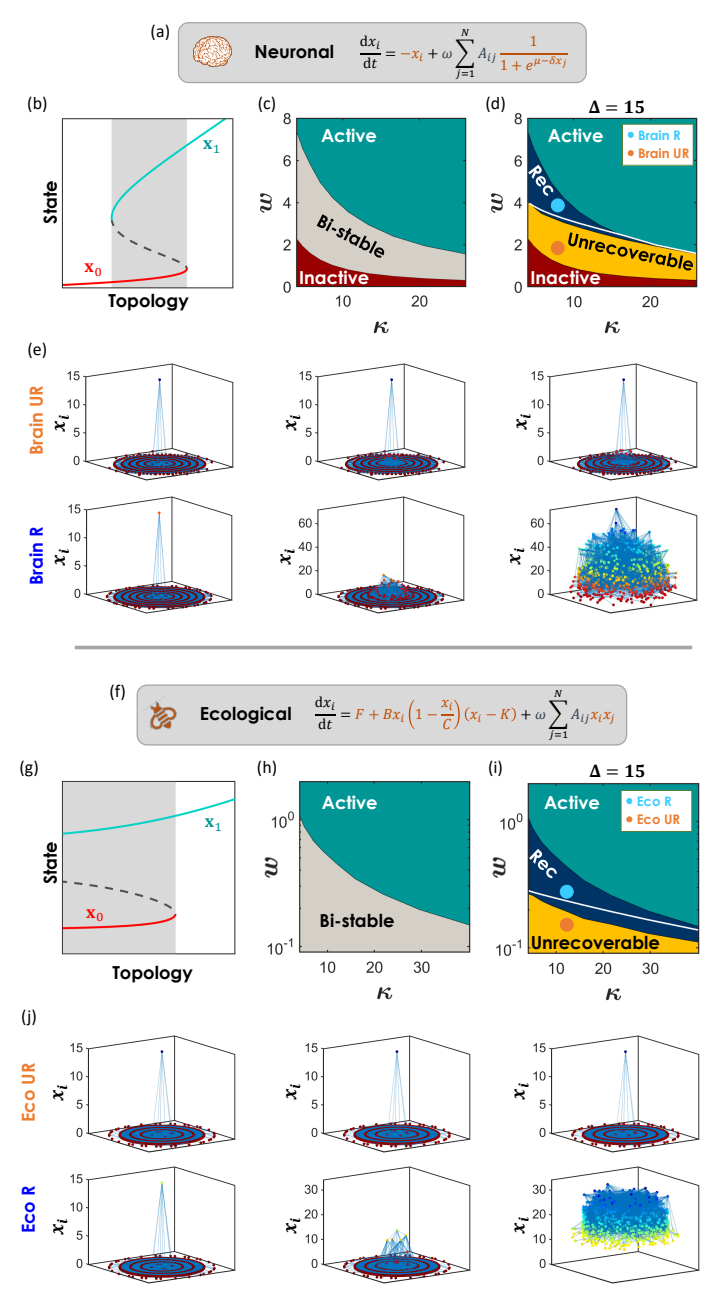


Figure 4: Recoverability of neuronal and ecological dynamics. (a) We model neuronal interactions via the Cowan-Wilson dynamics. (b) The system exhibits three phases: An inactive state \mathbf{x}_0 (red) when κ, ω are small, and an active state \mathbf{x}_1 (green) under large κ, ω . Between these two extremes we observe a bi-stable state (center, grey shaded) in which the system can reside in both \mathbf{x}_0 and \mathbf{x}_1 . (c) The κ, ω phase diagram, featuring the three states, inactive (red), bi-stable (grey) and active (green). (d) Our analysis predicts a new fourth phase, splitting the bi-stable state into two distinct dynamic phases - unrecoverable (yellow) vs. recoverable (blue). Simulation results (yellow-blue transition) are in good agreement with our theoretical prediction (white solid line). To test our prediction in an empirical setting we used our Brain network 49, diluted to reside in the bistable phase (Supplementary Section 4.4). The resulting network with $\kappa = 6.6$ was simulated under two values of ω : Brain UR with $\omega = 2$, which is unrecoverable (orange circle), and Brain R with $\omega = 4$ - recoverable (light blue circle). (e) Indeed, we find that Brain UR fails to reignite (top), while Brain R is successfully reactivated (bottom). Ecological dynamics. (f) We consider symbiotic ecological interactions. The self-dynamics is captured by migration (F) complemented by logistic growth and the Alley effect; the interaction follows the Lotka-Volterra response function 41 (Supplementary Section 3.3). (g) The system exhibits two phases: The active \mathbf{x}_1 (green) when κ, ω are large, and bi-stability of \mathbf{x}_1 and \mathbf{x}_0 (red) when κ, ω are reduced (grev shaded). (h) The κ, ω phase diagram. In the active phase (green) the system is guaranteed to reside in \mathbf{x}_1 , however in the bi-stable phase (grey) it can be in both states, and hence, within this phase, once collapsed, the system will not recover spontaneously. (i) Once again, our analysis shows that the bi-stable phase is split, giving rise to our new recoverable phase (blue). To further support this we used an empirical plant-pollinator network 51 (Eco, $\kappa = 11.1$, Supplementary Section 4.4) with two different weights: Eco UR ($\omega = 0.15$, unrecoverable, orange) and Eco R ($\omega = 0.3$, recoverable, light blue). (j) As predicted, Eco UR remains in \mathbf{x}_0 (top), while Eco R is successfully reignited (bottom).

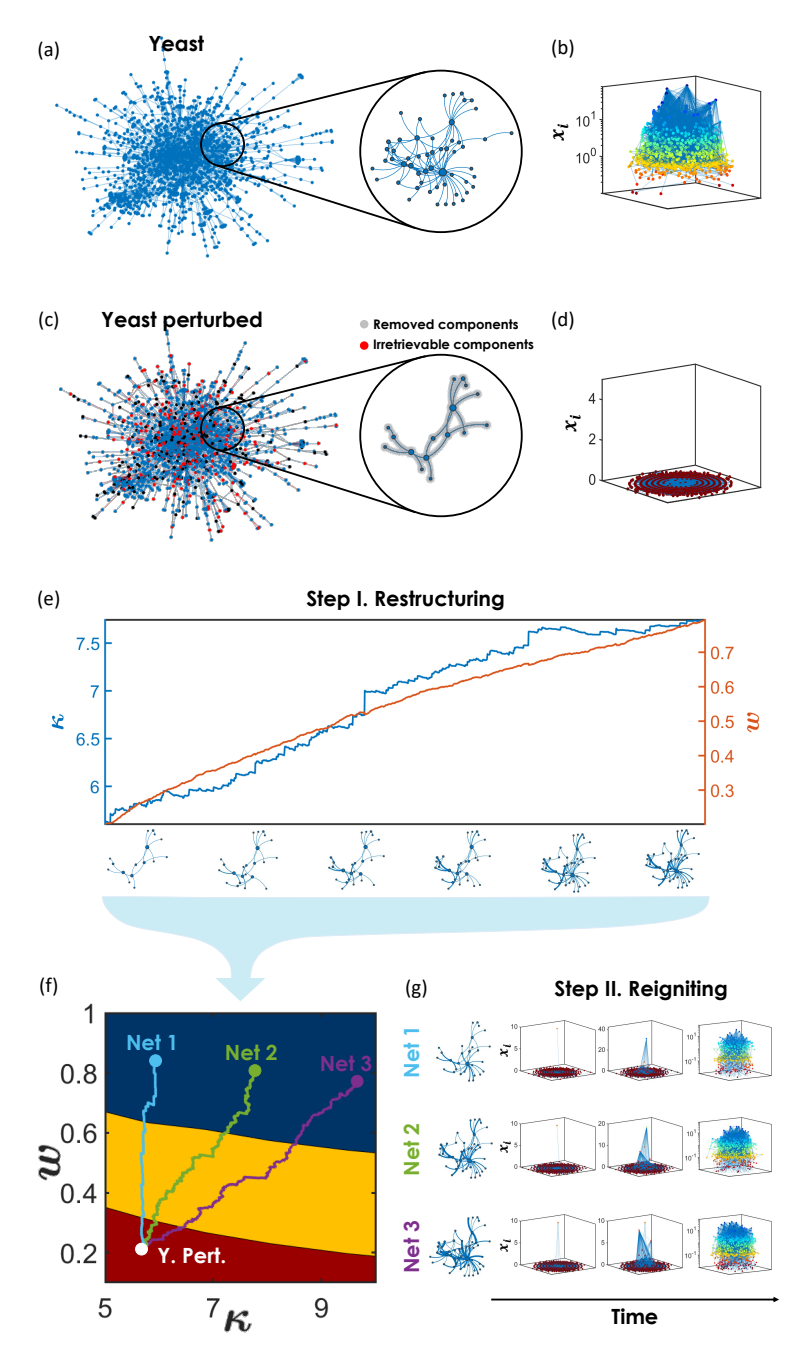


Figure 5: Two-step recovery for reviving a failed system. (a) The unperturbed Yeast protein interaction network. For visibility we focus on the circled sub-network. (b) The dynamic states x_i of all nodes. As expected, the unperturbed network is in the active state \mathbf{x}_1 , hence all $x_i > 0$. (c) - (d) Following extensive perturbation in which 30% of nodes and 30% of links (grey and red) were deleted the state of the network collapses to the inactive \mathbf{x}_0 , i.e. all $x_i = 0$. The challenge is that some of the deleted components (nodes/links) are inaccessible, and hence cannot be retrieved (red). This captures the restructuring constraints that are, indeed, inevitable in realistic scenarios. Circle at center - we focus on the same sub-network shown in (a), the unperturbed network components are highlighted, the deleted nodes links appear in grey and red. (e) Step I. Within the given constraints we restructure the network by reintroducing nodes/links or strengthening link weights. Such structural interventions can be mapped to their impact on the two relevant control parameters κ (blue) and ω (orange). Here we track a sequence of restructuring steps. For illustration, we show the highlighted sub-network in (c) as it restructures, acquiring nodes, links and increased weights (sub-networks along the x-axis). (f) Each such sequence of restructuring steps can be mapped into a path in the κ, ω phase diagram. A successful restructuring path must lead the network from the collapsed phase (red) into the recoverable phase (blue). Our predicted phase diagram helps us design several alternative paths, affording us the flexibility to, e.g., focus mainly on increasing weights ω (Net 1, light blue path) or also on enhancing network density κ (Net 3, purple path), all depending on the nature of our constraints. The resulting networks Net 1 - 3 may differ from the original unperturbed network, as indeed, our goal is not to simply reverse the damage, but to revive the system's dynamic activity. (e) Step II. Once the network is brought to the recoverable phase, we can revive it via single-node reigniting, demonstrated here on each of our restructured networks, Net 1 - 3.

FIGURES - FULL SIZE

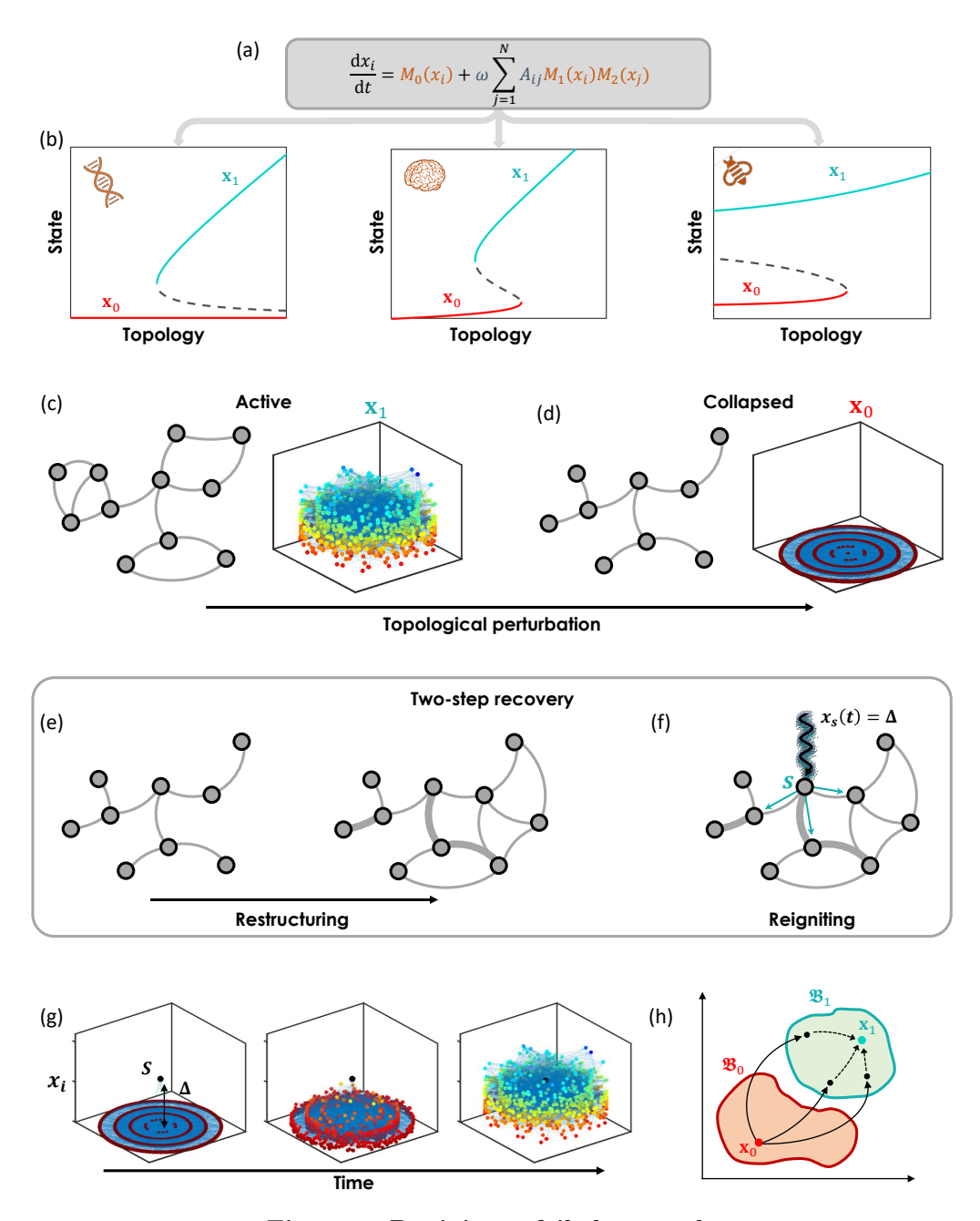


Figure 1. Reviving a failed network.

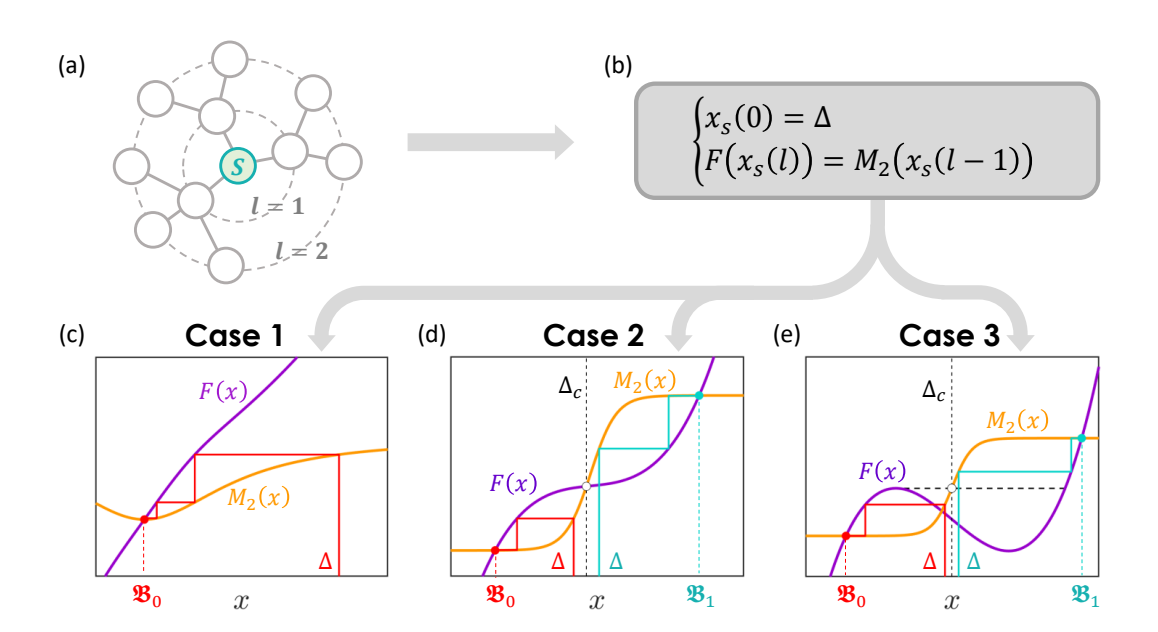


Figure 2. Can a system be reignited by a single node?

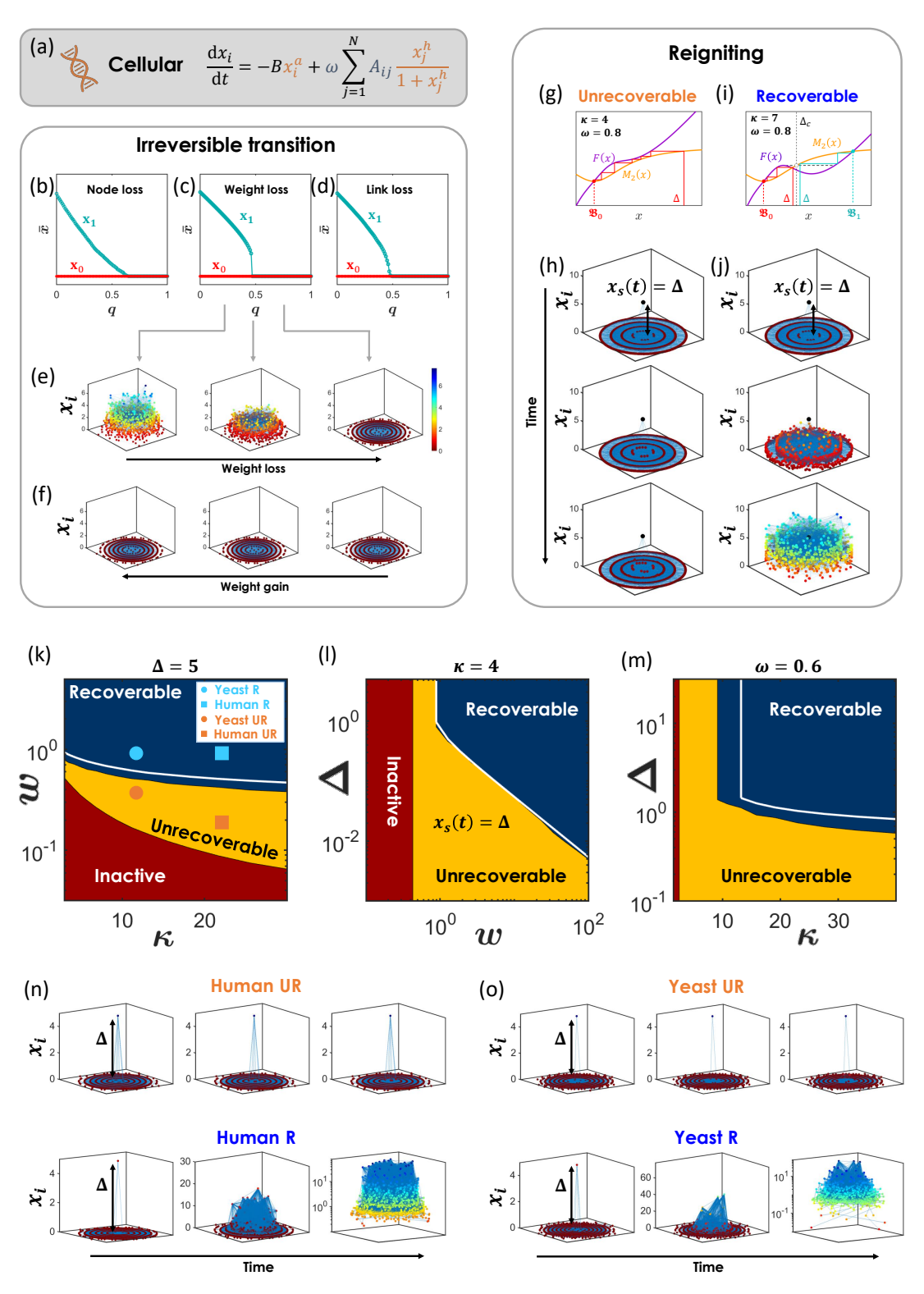


figure 3. Recoverability of cellular dynamics.

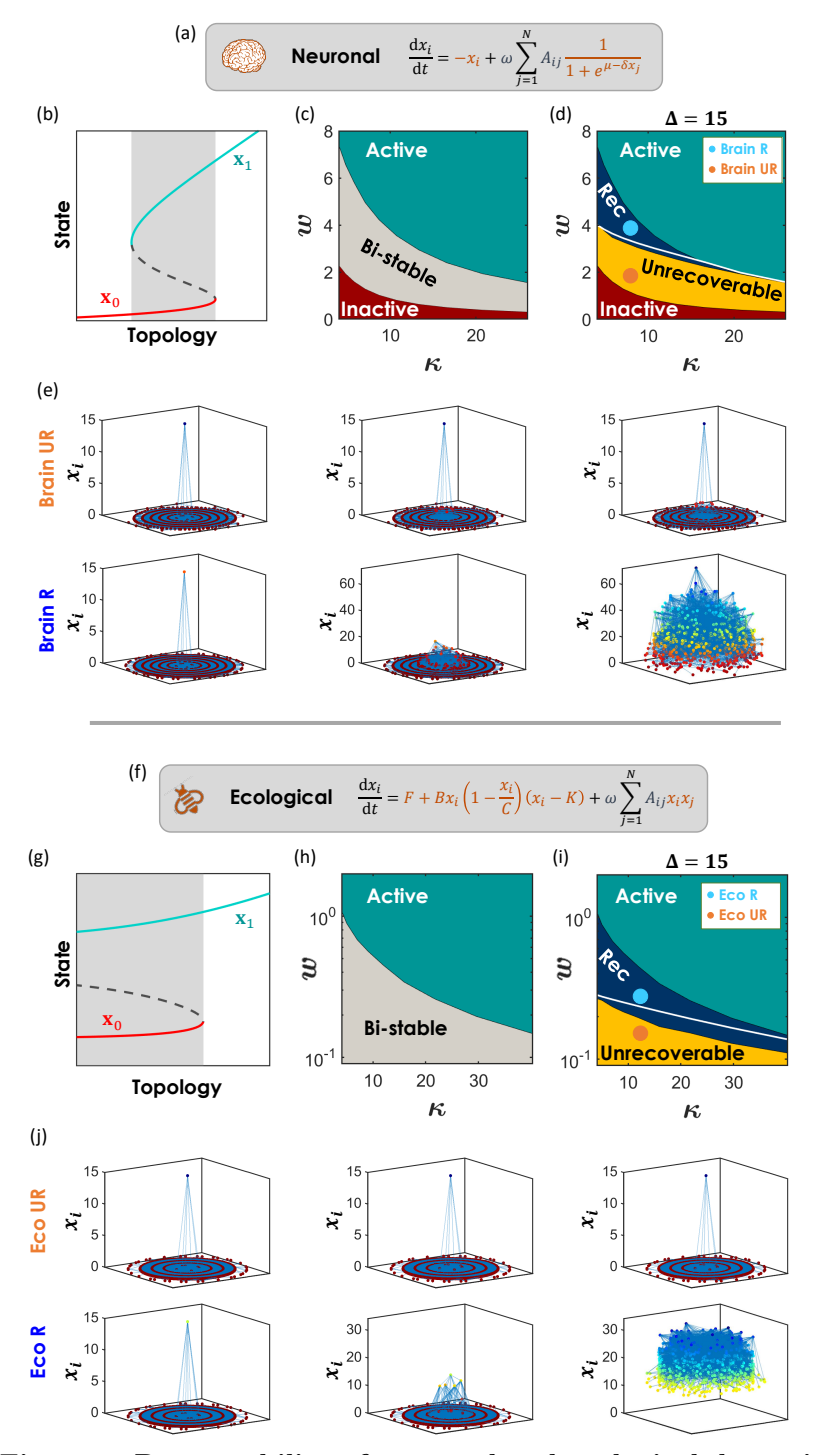


Figure 4. Recoverability of neuronal and ecological dynamics.

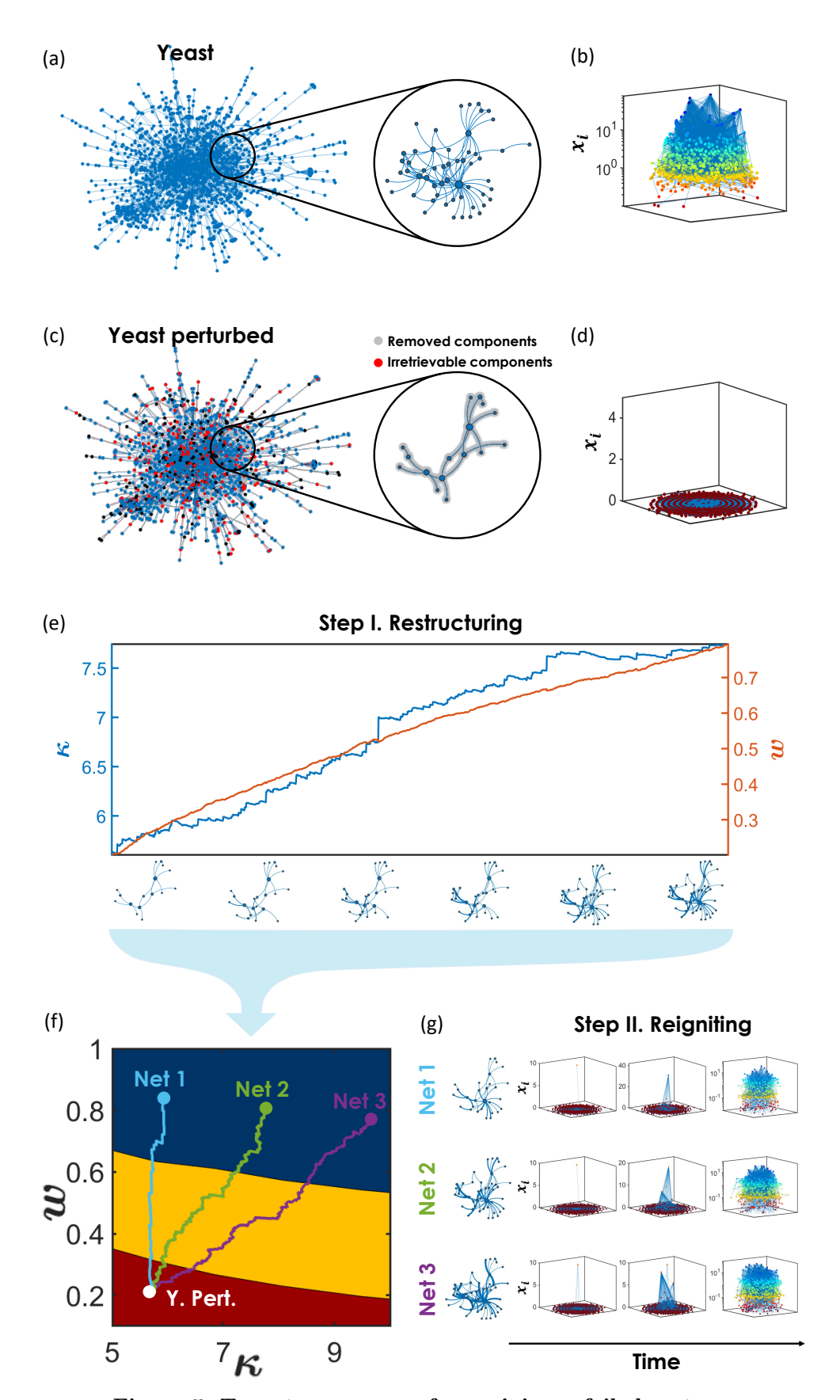


Figure 5. Two-step recovery for reviving a failed system.

Reviving a failed network via microscopic interventions

Supplementary information

December 1, 2020

Contents

1	Stea	ady-state analysis	1
2	Rec	coverability	5
	2.1	Modeling single-node reigniting	5
	2.2	Steady-state analysis	9
	2.3	Predicting the final shell states	10
3	Dyr	namic models	13
	3.1	Cellular dynamics	14
		3.1.1 Free system	14
		3.1.2 Reigniting	15
		3.1.3 The role of the Hill coefficient	16
	3.2	Neuronal dynamics	16
		3.2.1 Free system	17
		3.2.2 Reigniting	17
	3.3	Mutualistic population dynamics	18
		3.3.1 Free system	18
		3.3.2 Reigniting	19
4	Nur	merical analysis	21
	4.1	Numerical integration	21
	4.2	Reigniting	21
	4.3	Constructing the phase diagrams in Figs. 3-5	22
	4.4	Model and empirical networks	22

1 Steady-state analysis

While this is not the focus of the current contribution, as a prerequisite to discussing recoverability, we must first map the *natural* state-space of our systems, namely the dynamic state transitions that can be observed absent our reigniting interventions. To achieve this we use the theoretical framework published recently in Ref. [1], which incorporates mean-field analysis to predict (i) the potential states of the system \mathbf{x}_{α} , and (ii) the critical transition points between them. This framework allows a rather general treatment of a broad model family of dynamic models, under the assumption of weak degree correlations. Other formulations for steady-state analysis can be equally relevant, if, *e.g.*, degree correlations cannot be neglected.

We consider a class of systems captured by

$$\frac{\mathrm{d}x_i}{\mathrm{d}t} = M_0(x_i) + \omega \sum_{j=1}^N A_{ij} M_1(x_i) M_2(x_j), \tag{1.1}$$

where $x_i(t)$ is node i's dynamic activity $(i=1,\ldots,N)$ and the nonlinear functions $M_0(x)$, $M_1(x)$, $M_2(x)$ describe the system's intrinsic dynamics, i.e. its self-dynamics (M_0) and its interaction mechanisms (M_1, M_2) . The patterns of connectivity between the nodes are captured by the network A_{ij} , a binary $N \times N$ adjacency matrix, which we take to follow the configuration model framework, namely a random network with an arbitrary degree distribution, P(k). The average strength of all interactions is governed by the weight ω . Focusing on constructive interactions, in which nodes positively impact each others activity, we take $\omega M_1(x) \geq 0$ and $M_2(x) \geq 0$ and monotonous, excluding, e.g., negative interactions or oscillatory coupling functions.

The steady-states $\mathbf{x}_{\alpha} = (x_{\alpha,1}, \dots, x_{\alpha,N})^{\top}$ of Eq. (1.1) are obtained by setting its derivative on the left hand side to zero and satisfying linear stability. We focus here on systems with at least two steady-states, i.e. $\alpha = 0, 1$, one of which is desirable ($\alpha = 1$) and the otherundesirable ($\alpha = 0$). These states provide an N-dimensional descriptions of the system, capturing the stable activity $x_{\alpha,i}$ of all nodes $i=1,\ldots,N$. To obtain a macroscopic map of the different dynamic states of the system we use the mean-field approach described in Ref. [1]. This approach accounts for the potential diversity between individual nodes, i.e. P(k), but assumes their neighborhoods are statistically similar. Hence it captures the often encountered observation that real-world networks exhibit extreme levels of degree-heterogeneity, yet, based on the configuration model framework, it assumes negligible degree-correlations. This assumption, while approximate, has little impact on our observed results. Indeed, in our application in the main text, we examined our prediction on real-world networks (Eco, Brain, PPI), some which have been shown to feature measurable degree-correlations. Still, we find that our predictions are insensitive to these correlations, confirming that their secondary role in the context of recoverability, as they have no discernible impact on our observed results.

Using this mean-filed approach, we can now track the state of the system by its average nearest neighbor residual degree [1]

$$\kappa = \frac{1}{N} \sum_{i=1}^{N} \frac{1}{k_i} \sum_{j=1}^{N} A_{ij} k_j - 1.$$
 (1.2)

This captures the degree of a *typical* neighbor, and hence the average degree of each node's immediate interacting partners. We emphasize again, that while the number of direct neighbors of a node may be potentially diverse, often scale-free, the residual degree, obtained not from a *single*, but from a *sample* of nodes, is typically more homogeneous, and therefore succumbs to mean-field treatment.

We can now track the state of the system, by the average neighbor activity

$$\bar{\mathbf{x}} = \frac{1}{N} \sum_{i=1}^{N} \frac{1}{k_i} \sum_{j=1}^{N} A_{ij} x_j, \tag{1.3}$$

which using Eq. (1.1) follows

$$\frac{\mathrm{d}\bar{\mathbf{x}}}{\mathrm{d}t} = M_0(\bar{\mathbf{x}}) + \beta M_1(\bar{\mathbf{x}}) M_2(\bar{\mathbf{x}}), \tag{1.4}$$

where

$$\beta = (\kappa + 1)\omega \tag{1.5}$$

is the average neighbor's weighted degree. While the detailed derivation of (1.4) is provided in Ref. [1], the reader can intuitively observe that it captures the typical behavior of a node with degree β , *i.e.* a typical nearest neighbor.

The steady-state solutions of (1.4), denoted by $\bar{\mathbf{x}}_{\alpha}$, characterize the different fixed-points of the system. Hence, while the state \mathbf{x}_{α} provides the complete N-dimensional description of the system's steady-state activity, $\bar{\mathbf{x}}_{\alpha}$ in (1.3) reduces that into a single averaged quantity. The stability of each potential fixed-point is obtained from linear stability analysis, requiring

$$\frac{\mathrm{d}}{\mathrm{d}\bar{\mathbf{x}}} \left[M_0(\bar{\mathbf{x}}) + \beta M_1(\bar{\mathbf{x}}) M_2(\bar{\mathbf{x}}) \right] \Big|_{\bar{\mathbf{x}}_{\alpha}} < 0, \tag{1.6}$$

a negative derivative, ensuring that deviations from $\bar{\mathbf{x}}_{\alpha}$ decay exponentially. Satisfying (1.6), for a given state $\bar{\mathbf{x}}_{\alpha}$, depends on the value of β , and hence on A_{ij} and ω through (1.2) and (1.5). Equation (1.6), therefore, exposes the range of β values (if any) under which each fixed-point $\bar{\mathbf{x}}_{\alpha}$ is stable, linking the system's topology, A_{ij} , ω , to its observed dynamic states.

In **Box I** we demonstrate this analysis on cellular dynamics, obtaining the potential states and transitions of the gene-regulation, a specific system within our general Eq. (1.1). Cellular dynamics, we find, can sustain a stable active state only if A_{ij} is sufficiently dense (large κ) or if the link weights are sufficiently strong (large ω), together satisfying

$$\beta = (\kappa + 1)\omega > 2. \tag{1.12}$$

More broadly, this example illustrates the fundamental premise of our present analysis • The

Box I. Example. Cellular dynamics. As an example we consider gene-regulatory dynamics, captured by the Michaelis-Menten model [2], for which (1.1) takes the form

$$\frac{\mathrm{d}x_i}{\mathrm{d}t} = -Bx_i^a + \omega \sum_{j=1}^{N} A_{ij} \frac{x_j^h}{1 + x_j^h}.$$
 (1.7)

This dynamic equation maps into (1.1) through $M_0(x) = -Bx^a$, $M_1(x) = 1$ and $M_2(x) = x^h/(1+x^h)$. Using the mean-field approximation of (1.4) we write

$$\frac{\mathrm{d}\bar{\mathbf{x}}}{\mathrm{d}t} = -B\bar{\mathbf{x}}^a + \beta \frac{\bar{\mathbf{x}}^h}{1 + \bar{\mathbf{x}}^h},\tag{1.8}$$

which, under $d\bar{\mathbf{x}}/dt = 0$, predicts

$$\beta = B\bar{\mathbf{x}}^a \left(1 + \frac{1}{\bar{\mathbf{x}}^h}\right),\tag{1.9}$$

as shown in Fig. 3b. Setting B=1, a=1 and h=2 (see Ref. [1] for a more general treatment), we extract $\bar{\mathbf{x}}$ from (1.9, predicting three fixed-points (Fig. 3b): The inactive $\bar{\mathbf{x}}_0=0$ (undesirable, red), the active $\bar{\mathbf{x}}_1=\beta/2+\sqrt{(\beta/2)^2-1}$ (desirable, green), and the intermediate $\bar{\mathbf{x}}_2=\beta/2-\sqrt{(\beta/2)^2-1}$ (grey dashed-line).

Next we test the dynamic stability of each of these three solutions via Eq. (1.6), providing the stability condition

$$-aB\bar{\mathbf{x}}^{a-1} + \beta \frac{h\bar{\mathbf{x}}^{h-1}}{(1+\bar{\mathbf{x}}^h)^2} < 0. \tag{1.10}$$

Using our selected parameters B = a = 1, h = 2 condition (3.5) reduces to

$$-\left(1+\bar{\mathbf{x}}^2\right)^2+2\beta\bar{\mathbf{x}}<0,\tag{1.11}$$

from which we can directly obtain the system's state phase-diagram. For the inactive $\bar{\mathbf{x}}_0 = 0$ we have the left hand side of (1.11) being -1, independently of β , and hence this state is unconditionally stable. The stability of the other to states is obtained by substituting $\bar{\mathbf{x}}_1$ and $\bar{\mathbf{x}}_2$ into (1.11), finding that $\bar{\mathbf{x}}_2$ is never stable, and hence it does not represent a potential state of the system, while the desirable $\bar{\mathbf{x}}_1$ is stable under the condition that $\beta > 2$ (Fig. 3b). Therefore $\beta < 2$ forces a collapse on to \mathbf{x}_0 , while $\beta > 2$ represents a bi-stable phase, where the system can reside in both \mathbf{x}_0 and \mathbf{x}_1 , depending on initial conditions.

potential states of the system and the critical transitions between them, i.e. the system's phase diagram, are determined by its intrinsic dynamics $M_0(x)$, $M_1(x)$ and $M_2(x)$ • The specific state of a given system, however, i.e. where it resides along that phase diagram, is predicted by the weighted network topology via A_{ij} , as encapsulated within κ (1.2), and via ω , as appears in (1.1) • Transitions between these states can occur as a result of perturbations to A_{ij} or ω . When such transitions occur, they are often irreversible, as we discuss below.

Irreversibility. The structure of the Eq. (1.7)'s stability diagram (Fig. 3b) indicates that it is prone to irreversible collapse. Consider a system residing at the desirable \mathbf{x}_1 state, then driven towards \mathbf{x}_0 through a series of topological perturbations that resulted in $\beta < 2$.

The intuitive approach is to recover the system's topology and return the system to $\beta > 2$. However, since \mathbf{x}_0 is always stable, regardless of the value of β , the system will remain in \mathbf{x}_0 even after such topological reconstruction. Its recoverability, therefore, mandates dynamic intervention or reigniting, as we derive in Sec. 2. Hysteresis phenomena, such as this, where systems avoid spontaneous recovery, arise quite commonly in dynamics within the form (1.1). We therefore, seek to characterize our ability to dynamically reignite a failed system via parsimonious dynamic interventions.

Basins of attraction. In the bi-stable phase, the state of the system \mathbf{x}_0 or \mathbf{x}_1 depends on the initial condition $x_i(t=0)$. This splits the N-dimensional state space of the system \mathbf{x} into basins

$$\mathfrak{B}_{\alpha} = \left\{ \mathbf{x}(t=0) \mid \mathbf{x}(t\to\infty) = \mathbf{x}_{\alpha} \right\}$$
 (1.13)

which comprise all initial conditions from which Eq. (1.1) converges to the fixed-point \mathbf{x}_{α} . In Fig. 3b we show the projection of the two relevant basins \mathfrak{B}_0 and \mathfrak{B}_1 onto the one-dimensional space of $\bar{\mathbf{x}}$. Here an initial conditions in which $\bar{\mathbf{x}} > \bar{\mathbf{x}}_2$ (grey dashed-line) will converge to $\bar{\mathbf{x}}_1$ (up pointing arrows), while $\bar{\mathbf{x}} < \bar{\mathbf{x}}_2$ will lead to $\bar{\mathbf{x}}_0$ (down pointing arrows). Reigniting a system's failed dynamics, therefore, translates to steering it from the *state* \mathbf{x}_0 to the *basin* \mathfrak{B}_1 .

2 Recoverability

2.1 Modeling single-node reigniting

Consider a system of the type discussed above, characterized by two stable states - an undesirable \mathbf{x}_0 and a desirable \mathbf{x}_1 . Let us further assume that the system is in the bi-stable phase, presently at the undesirable \mathbf{x}_0 . We seek dynamic interventions, preferably minimal in nature, that will help us drive the system towards \mathbf{x}_1 . To achieve this we assign a selected set of nodes \mathcal{F} - the *forced* nodes - whose dynamics we externally control. This, effectively, changes the system's dynamics (1.1) into

$$\begin{cases} x_i = f_i(t) & i \in \mathcal{F} \\ \frac{\mathrm{d}x_i}{\mathrm{d}t} = M_0(x_i) + \omega \sum_{j=1}^N A_{ij} M_1(x_i) M_2(x_j) & i \notin \mathcal{F} \end{cases}, \tag{2.1}$$

in which nodes in \mathcal{F} are forced to follow the external control function $f_i(t)$, while the remaining $N - |\mathcal{F}|$ nodes continue to evolve via the system's natural interaction dynamics. In a realistic reigniting scenario we require $|\mathcal{F}| \ll N$ and $f_i(t)$ to be described by preferably simple functions, capturing the fact that often we have limited access or control over the dynamic behavior of the majority of the nodes. Taken to the limit, we choose

$$\mathcal{F} = \{s\},\tag{2.2}$$

a single forced source node, and

$$f_s(t) = \Delta, \tag{2.3}$$

a time-independent forcing function.

Such single node reigniting is, in principle, no different than reigniting by few nodes, since, for a large network, the immediate neighborhoods of each two randomly selected nodes have negligible overlap. Therefore, the impact of one node's forced activity has little interference with that of the other. In other words, for a randomly selected microscopic set of nodes, the group \mathcal{F} will be, most probably, spread throughout the network, comprising an isolated set of reigniting focal points, each impacting only its local neighborhood (Fig. 1a). Under these conditions, the forcing of more than one node does not significantly contribute to the reigniting, and only begins to take effect if the recovered neighbors from one forced node overlap with those of another. Such overlap occurs only if each of the forced nodes has by itself reignited a large fraction of inactive nodes, which, in principle depicts an independent set of single-node reigniting instances. Therefore reigniting via $|\mathcal{F}| \ll N$ is, asymptotically identical to reigniting via $|\mathcal{F}| = 1$ - a single forced activity focal point that must penetrate the network and impact its distant neighbors towards the basin \mathfrak{B}_1 .

To evaluate the impact of s's forcing we track the response of the shells

$$K_s(l) = \{ i \in (1, \dots, N) | L_{is} = l \},$$
 (2.4)

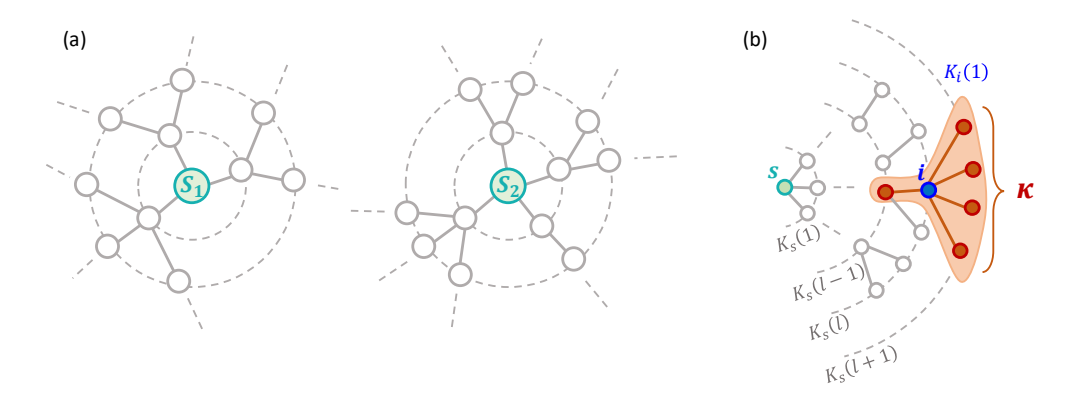


Figure 1: How a single node impacts the network. (a) Reigniting by two nodes s_1, s_2 (or any microscopic fraction of nodes) introduces two focal points of reactivation into the network. For a large network, the adjacent shells around s_1 and s_2 have little overlap, hence each only impacts its local neighborhood. Under these conditions s_1 's forcing does not meaningfully reinforce that of s_2 , and each behaves as an independent single-node reigniting source. In case s_1 is able to excite the distant shells, to the extent that its impact interferes with that of s_2 , this indicates that s_1 's activation had a non-local impact. This is the case where s_1 indeed successfully reignites the entire system. Therefore, we find that reigniting by a microscopic random of nodes is, in effect, no different that reigniting with a single node. (b) The impact of our reigniting at s on a node s is mediated by s direct neighborhood s in a large random network, whose structure is locally tree-like, this neighborhood has typically a single node in s in s closer to the source, and s nodes in s in s in the recurrence relation of Eq. (2.18).

comprising all nodes whose shortest path to s, L_{is} , is of length l. We have $K_s(0) = \{s\}$, $K_s(1) = s$'s group of direct neighbors, $K_s(2)$ its second neighbors, etc. The average activity in $K_s(l)$ is captured by

$$x_s(l,t) = \frac{1}{|K_s(l)|} \sum_{i \in K_s(l)} x_i(t), \tag{2.5}$$

allowing us to evaluate the impact of the forcing $x_s(t) = \Delta$ at any distance l from s.

Being initially at the undesired state we begin with $x_s(l, t = 0) = \bar{\mathbf{x}}_0$ for all l > 0; for l = 0 we set $x_s(l = 0, t) = \Delta$, as per our forcing intervention. In a non-recoverable system the s-forcing fails to reignite the system, its impact remains local, and hence the distant shells continue to be in the undesired state's basin of attraction, namely

$$x_s(l \to \infty, t \to \infty) \in \mathfrak{B}_0. \tag{2.6}$$

Conversely, if the system is recoverable, s's forcing penetrates the network to impact the entire system, thus leading to

$$x_s(l \to \infty, t \to \infty) \in \mathfrak{B}_1,$$
 (2.7)

in which the distant shells have been successfully reignited. Under these conditions we can

terminate our forcing, to allow s's local neighborhood, whose state is frozen by our external intervention, to also transition to \mathbf{x}_1 via the system's natural, undisturbed, dynamics.

To obtain a direct set of equations for $x_s(l,t)$ in (2.5), we write

$$\frac{\mathrm{d}x_s(l,t)}{\mathrm{d}t} = \frac{1}{|K_s(l)|} \sum_{i \in K_s(l)} \frac{\mathrm{d}x_i}{\mathrm{d}t}, \qquad (2.8)$$

which using (1.1) to express the r.h.s. derivative provides

$$\frac{\mathrm{d}x_s(l,t)}{\mathrm{d}t} = \frac{1}{|K_s(l)|} \sum_{i \in K_s(l)} \left(M_0(x_i) + \omega \sum_{j=1}^N A_{ij} M_1(x_i) M_2(x_j) \right). \tag{2.9}$$

To approximate the summations over $M_0(x_i)$ and $M_1(x_i)$ we use a mean-field approach, writing

$$\frac{1}{|K_s(l)|} \sum_{i \in K_s(l)} M_q(x_i(t)) \approx M_q(x_s(l,t))$$
(2.10)

for q=0,1, namely we take $\langle M_q(x)\rangle\approx M_q(\langle x\rangle)$. This approximation is exact if at least one of the following two conditions applies: (i) $M_0(x)$ and $M_1(x)$ are linear; (ii) $x_i(t)$ are uniform within the shell $K_s(l)$. Clearly, these conditions are not guaranteed, however, under many practical scenarios, they represent a sufficient approximation, designed to detect the macroscale behavior of the system - as fully corroborated by our numerical examination. Indeed, while Eq. (1.1) is, generally, nonlinear, its components, $M_0(x)$, $M_1(x)$, in many of the useful models, are often sub-linear, linear or weakly super-linear, i.e. involving powers that are not much higher than unity. This satisfies, approximately, condition (i). In other cases we may observe strong nonlinearities in $M_0(x)$ and $M_1(x)$, e.g., in our ecological dynamics, but in such cases, we often have bounded activities $x_i(t)$. This ensures a narrow distribution of $x_i(t)$, roughly satisfying condition (ii). We further elaborate on the relevance of these condition in the appropriate sections, where we analyze each of our specific dynamic systems (Sec. 3). Using approximation (2.10), we rewrite (2.9) as

$$\frac{\mathrm{d}x_s(l,t)}{\mathrm{d}t} = M_0(x_s(l,t)) + \omega M_1(x_s(l,t)) \frac{1}{|K_s(l)|} \sum_{i \in K_s(l)} \sum_{j \in K_i(1)} M_2(x_j), \tag{2.11}$$

where we have also replaced the original summation notation $\sum_{j=1}^{N} A_{ij} \cdots$ by $\sum_{K_i(1)} \cdots$, a summation of *i*'s nearest neighbors $K_i(1)$.

Consider the group $K_i(1)$ in the summation of (2.11). It involves all nodes j that are nearest neighbors of a node $i \in K_s(l)$. Therefore, by definition, we have j in either $K_s(l-1), K_s(l)$ or $K_s(l+1)$, namely

$$j \in \bigcup_{n=-1}^{+1} K_s(l+n). \tag{2.12}$$

We denote the fraction of nodes in each of these three shells, l-1, l and l+1, by [3]

$$\epsilon_n = \frac{1}{|K_s(l)|} \sum_{i \in K_s(l)} \frac{|K_i(1) \cap K_s(l+n)|}{|K_i(1)|},\tag{2.13}$$

where n = -1, 0, 1. This captures, for the average node $i \in K_s(l)$, how many of its direct neighbors, $K_i(1)$, are in the $K_s(l-1)$, $K_s(l)$ or $K_s(l+1)$ shells (Fig. 1b). We can now express the sum over $j \in K_i(1)$ in (2.11) as

$$\sum_{j \in K_i(1)} M_2(x_j) \approx \sum_{n=-1}^{+1} \epsilon_n |K_i(1)| M_2(x_s(l+n,t)), \tag{2.14}$$

splitting the terms among the three groups in $K_s(l+n)$, each with its respective fraction ϵ_n . We, once again, used the mean-field approximation to introduce the averaged $x_s(l+n,t)$ into the function $M_2(x)$. An elaborate and rigorous derivation of (2.14) can be found in Ref. [3].

For a large random network, *i.e.* configuration model, the topology is known to be locally tree-like, featuring a vanishing number of loops [4]. Under these conditions, the average node i in $K_s(l)$ has, typically, a single link to a node in $K_s(l-1)$ and no links to any nodes in $K_s(l)$ itself, such that all its remaining $|K_i(1)| - 1$ links reach nodes in $K_s(l+1)$. Also within this model, nodes in any shell $K_s(l)$, l > 0, follow the residual degree distribution, and hence, on average, their degree is $\kappa + 1$, with κ taken from (1.2), namely

$$\frac{1}{|K_s(l)|} \sum_{i \in K_s(l)} |K_i(1)| = \kappa + 1. \tag{2.15}$$

Together, this predicts that (Fig. 1b)

$$\epsilon_{-1} = \frac{1}{\kappa + 1}, \quad \epsilon_0 = 0, \quad \epsilon_{+1} = \frac{\kappa}{\kappa + 1},$$

$$(2.16)$$

a result, once again, derived in detail in Ref. [3]. We now use (2.15) and (2.16) to substitute (2.14) into (2.11), obtaining

$$\frac{\mathrm{d}x_s(l,t)}{\mathrm{d}t} = M_0(x_s(l,t)) + \omega M_1(x_s(l,t)) \Big(M_2(x_s(l-1,t)) + \kappa M_2(x_s(l+1,t)) \Big). \tag{2.17}$$

Equation (2.17) expresses the dynamics of the average activity in the l-shell, as driven by the system's internal dynamic mechanisms $M_0(x), M_1(x)$ and $M_2(x)$. It uses the tree-like structure of the network shells to reduce the detailed network topology A_{ij} in (2.1) to a simplified form, focusing on the average node in $K_s(l)$, which, typically, interacts with a single node in $K_s(l-1)$ and κ residual nodes in $K_s(l+1)$. This equation is valid for all shells $K_s(l)$ at l>0; for $K_s(0)$ we use the first equation of (2.1), providing $x_s(0,t)=\Delta$. Together we arrive at Eq. (5) of the main text

$$\begin{cases} x_s(0,t) = \Delta \\ \frac{dx_s(l,t)}{dt} = M_0(x_s(l,t)) + \omega M_1(x_s(l,t)) \Big(M_2(x_s(l-1,t)) + \kappa M_2(x_s(l+1,t)) \Big) \end{cases},$$
(2.18)

capturing the time evolution of nodes at distance l from the forced s; the initial condition is set to $x_s(l, t = 0) = \bar{\mathbf{x}}_0$ for all l > 0.

2.2 Steady-state analysis

To expose the long term behavior of (2.18) we seek its steady-state, obtained by setting the derivative on its left hand side to zero, namely

$$\begin{cases} x_s(0) = \Delta \\ 0 = M_0(x_s(l)) + \omega M_1(x_s(l)) \Big(M_2(x_s(l-1)) + \kappa M_2(x_s(l+1)) \Big) \end{cases}$$
 (2.19)

Note that we have now omitted the term t from $x_s(l,t)$, focusing on the steady-state

$$x_s(l) = x_s(l, t \to \infty), \tag{2.20}$$

i.e. the system's final, long term, activity patterns. To isolate $x_s(l)$ we rewrite the second equation in (2.19) as

$$R(x_s(l)) = \omega M_2(x_s(l-1)) + \omega \kappa M_2(x_s(l+1)), \qquad (2.21)$$

where

$$R(x) = -\frac{M_0(x)}{M_1(x)}. (2.22)$$

This, by inversion, provides

$$x_s(l) = R^{-1} \left(\omega M_2(x_s(l-1)) + \omega \kappa M_2(x_s(l+1)) \right),$$
 (2.23)

a direct expression of $x_s(l)$ in function of its two neighboring terms, $x_s(l \pm 1)$.

We can now substitute (2.23) into the second equation in (2.19) to transform it into a second order recurrence relation, obtaining

$$\begin{cases} x_s(0) = \Delta \\ x_s(l) = R^{-1} \left(\omega M_2 \left(x_s(l-1) \right) + \omega \kappa M_2 \left(x_s(l+1) \right) \right) \end{cases}$$
 (2.24)

The challenge is that the recurrence (2.24) is ill-defined, as we only have one boundary

condition, $x_s(0) = \Delta$, instead of the two anchoring points required to obtain a unique solution. Hence, in and of itself, Eq. (2.24) cannot predict the final shell states $x_s(l)$, and therefore it is insufficient to determine if our reigniting is successful or not. Next, we introduce an approximate approach that allows us to track the desired fixed-points of (2.24).

2.3 Predicting the final shell states

While in general (2.24) is under-determined, we can use our prior knowledge on the states of Eq. (1.1) to constrain its potential solutions. Indeed, knowing that our system has potentially two stable fixed-points, \mathbf{x}_0 and \mathbf{x}_1 , we assume that our forcing at $x_s(0)$ can lead, asymptotically, to only two outcomes: successful reigniting, in which

$$x_s(l \to \infty) \in \mathfrak{B}_1,\tag{2.25}$$

or unsuccessful reigniting, where

$$x_s(l \to \infty) \in \mathfrak{B}_0. \tag{2.26}$$

Therefore, we do not need to solve the recurrence relation fully, just to determine whether it assumes the asymptotic solution (2.25) or (2.26).

We begin by expressing $x_s(l+1)$ in (2.24) as

$$x_s(l+1) = R^{-1} \left(\omega M_2(x_s(l)) + \omega \kappa M_2(x_s(l+2)) \right),$$
 (2.27)

obtained by substituting l by l+1 in the recurrence relation. This allows us to rewrite the recursive series as

$$\begin{cases}
 x_s(0) = \Delta \\
 x_s(l) = R^{-1} \left(\omega M_2 (x_s(l-1)) + \omega \kappa M_2 \left(R^{-1} \left(\omega M_2 (x_s(l)) + \omega \kappa M_2 (x_s(l+2)) \right) \right) \right), \\
 (2.28)
\end{cases}$$

expressing the term $x_s(l+1)$ in (2.24) via Eq. (2.27). This step provides $x_s(l)$ in terms of $x_s(l-1)$, $x_s(l)$ and $x_s(l+2)$. Consequently, the average activity at $K_s(l)$ is impacted by the state of the directly neighboring shell $K_s(l-1)$, by the equidistant nodes at $K_s(l)$ itself, and by the indirectly interacting second neighbors at $K_s(l+2)$. Our main assumption is that of these three effects - the first two, which represent $K_s(l)$'s direct neighborhood, supersede that of the third $x_s(l+2)$ term. Indeed, this term captures the state of the distant shell $K_s(l+2)$ whose impact on $x_s(l)$ is marginal as compared to the other two terms. We therefore approximate this term by

$$x_s(l+2) \approx \bar{\mathbf{x}}_0,\tag{2.29}$$

assuming this distant shell has not been significantly impacted by our reigniting, hence still

at its initial state \mathbf{x}_0 , having on average activity $\bar{\mathbf{x}}_0$. The activity $\bar{\mathbf{x}}_0$ can be obtained from Eq. (1.4) as explained in Sec. 1. This discrepancy, we expect, will have little impact on the accuracy of $x_s(l)$, as it only applies to l's distant neighbors. Using (2.29) to rewrite (2.28) we now have

$$x_s(l) = R^{-1} \left(\omega M_2 \left(x_s(l-1) \right) + \omega \kappa M_2 \left(R^{-1} \left(\omega M_2 \left(x_s(l) \right) + \omega \kappa M_2 (\bar{\mathbf{x}}_0) \right) \right) \right), \qquad (2.30)$$

from which we can extract $x_s(l)$ as

$$\frac{1}{\omega}R(x_s(l)) - \kappa M_2\left(R^{-1}\left(\omega M_2(x_s(l)) + \omega \kappa M_2(\bar{\mathbf{x}}_0)\right)\right) = M_2(x_s(l-1)). \tag{2.31}$$

Finally, our recurrence relation (2.28) converges to the form of Eqs. (7) and (8) of the main text, providing

$$\begin{cases} x_s(0) = \Delta \\ F(x_s(l)) = M_2(x_s(l-1)) \end{cases}, \tag{2.32}$$

where

$$F(x) = \frac{1}{\omega}R(x) - \kappa M_2 \left(R^{-1} \left(\omega M_2(x) + \omega \kappa M_2(\bar{\mathbf{x}}_0)\right)\right). \tag{2.33}$$

These equations approximate the original second order recurrence of Eq. (2.24), by an approximate first order recurrence relation, now solvable using standard tools for analyzing recurrence relations, as outlined in the main text. First, we extract the fixed points of the recursion via [5]

$$F(x) = M_2(x). (2.34)$$

Maintaining consistency with the original dynamics (1.1), from which (2.32) is derived, the fixed point obtained via (2.34) must, by definition coincide with the intrinsic fixed-points $\bar{\mathbf{x}}_{\alpha}$ of the system. Indeed, our reigniting may either fail, leading to $\bar{\mathbf{x}}_0$, or succeed, arriving at $\bar{\mathbf{x}}_1$. It cannot, however, lead to any other points, which are not within the potential states intrinsic to (1.1). Hence the condition (2.34) may have only two outcomes: the system is non-recoverable if (2.34)'s only stable fixed-point is $\bar{\mathbf{x}}_0$. However, if it also features a stable $\bar{\mathbf{x}}_1$, then we can use the structure of F(x) and $M_2(x)$ to obtain the critical Δ_c above which (2.32) converges to $\bar{\mathbf{x}}_1$, and hence successfuly reignites. Hence, analyzing the intersection/s of F(x) and $M_2(x)$ we can predict the system's recoverability, and if recoverable, the required critical forcing.

Cobweb plots (Fig. 2). We solve the recurrence relation of (2.32) using cobweb plots [6]. Starting from an initial setting of $x_s(0) = \Delta$ we track the evolution of the recurrence. First obtaining $M_s(\Delta)$ (vertical path), then shifting horizontally to F(x), extracting $x_s(1)$. Continuing the process we observe weather the recurrence converges to \mathfrak{B}_0 or to \mathfrak{B}_1 . In case

the function F(x) is non-monotonic, this process may lead to convergence ambiguity, as illustrated in Case 3 of Fig. 2c, with both red and green pathways enabled. Such ambiguity is, of course, a mathematical artifact, as the real system in (1.1) will indeed follow only one of the potential tracks, not both. In reality, as we employ our reigniting from an initial condition which is in \mathfrak{B}_0 , the system, under any such instance of ambiguity, will converge back to \mathfrak{B}_0 , namely, it will select the red path and not recover. To remove this duality we use the construction of Fig. 2d, in which we introduce a plateau along the non-monotonic range in F(x). The corrected F(x) (solid purple line) is now monotonic and we can unambiguously analyze it via the proposed cobweb plots.

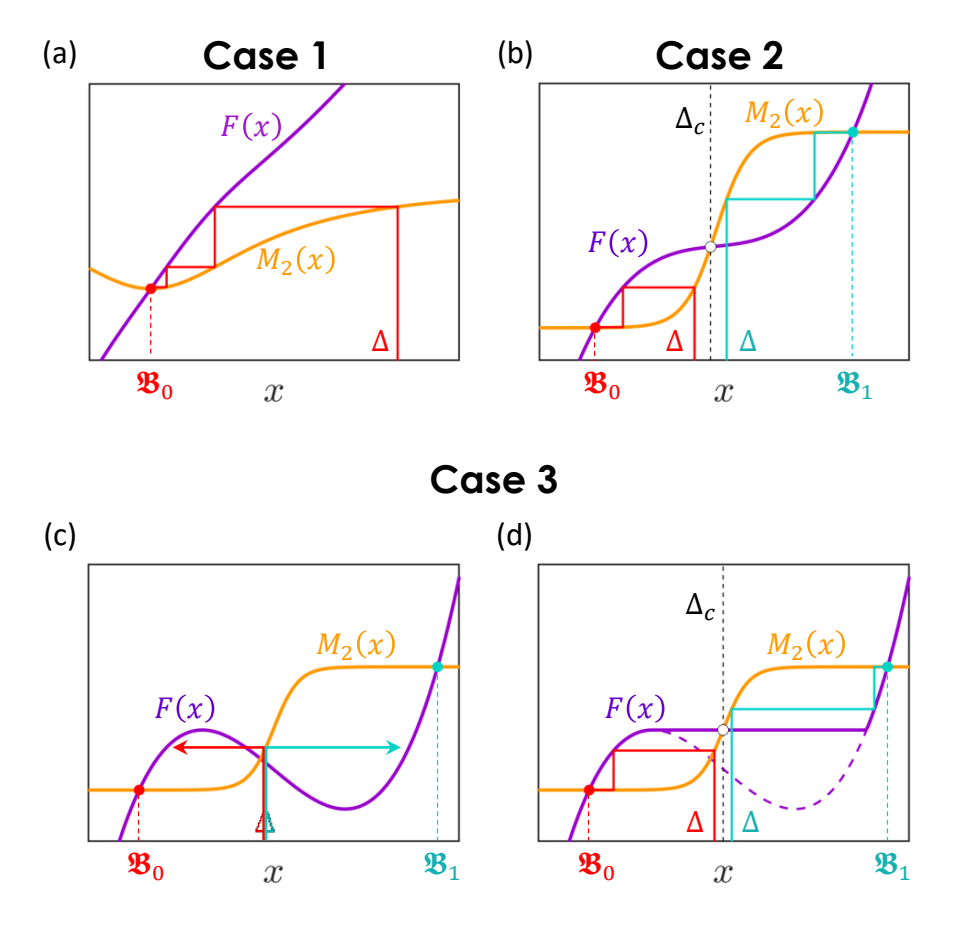


Figure 2: Solving the recurrence relation via cobweb plots. To solve (2.32) we begin at $x_s(0) = \Delta$, then track the recurrence by following the value of $M_2(x)$ (vertical steps) and equating this with F(x) (horizontal steps), as per the second equation in (2.32). (a) Case 1. Regardless of the starting point Δ , the system unconditionally converges to \mathfrak{B}_0 , and hence it is unrecoverable (red path). (b) Case 2. For $\Delta > \Delta_c$ the system reaches \mathfrak{B}_1 , i.e. recoverable (green path). (c) Case 3. In case F(x) is non-monotonic we encounter dual solutions, in which both the red and green pathways coexist. The real system, i.e. Eq. (1.1, however, will only follow the red path of the failed reigniting, as its initial condition is of all nodes residing in \mathfrak{B}_0 . (d) To treat this ambiguity we reconstruct F(x) by introducing a plateau over the non-monotonic range, leading to the monotonic F(x) (purple solid line) instead of the original function (purple-dashed line).

3 Dynamic models

To demonstrate our framework we examined the recoverability of three dynamic systems within the form of Eq. (1.1). Below we detail the analytical treatment of each of these systems, starting from the *free system*, in which we examine the states of the system absent our forcing Δ , then treating the *reignited system*, in which we introduce our single-node activation.

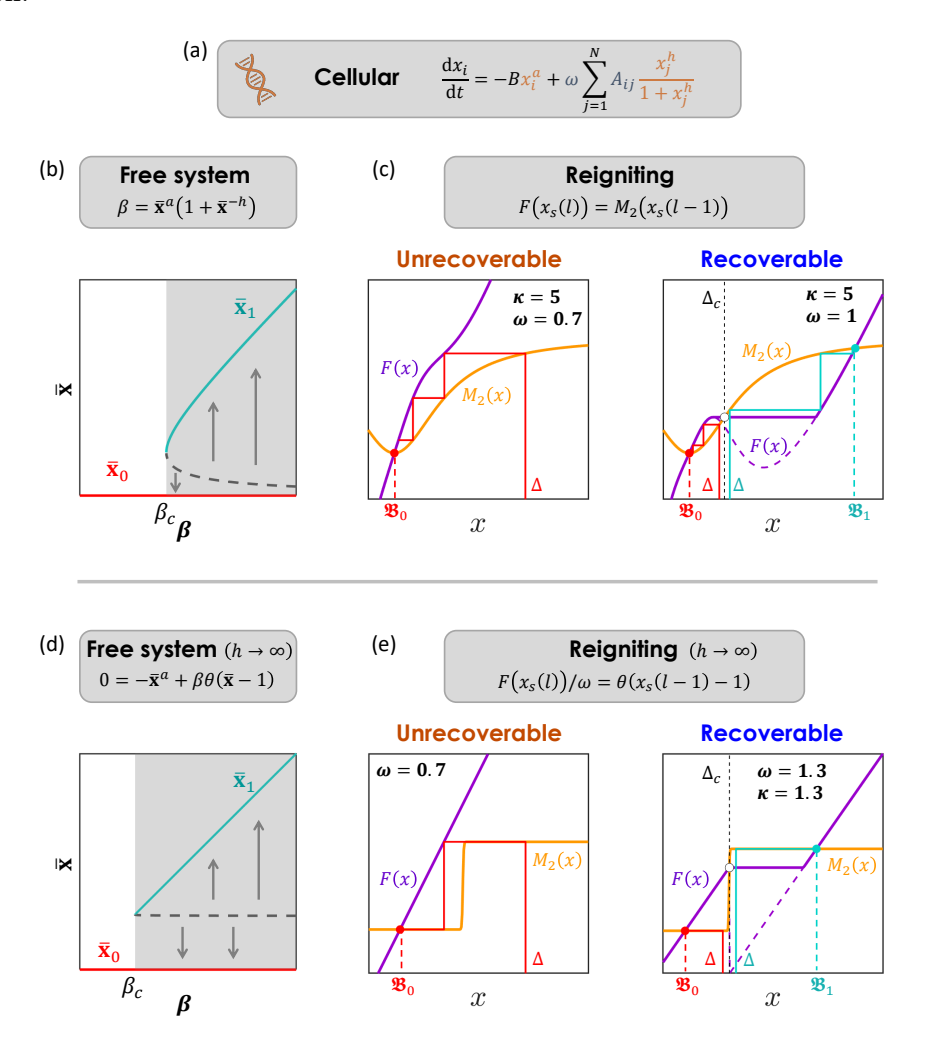


Figure 3: Cellular dynamics. (a) The Michaelis-Menten model for gene-regulation. (b) The fixed-point, inactive (red), vs. active (green), as obtained from Eq. (3.4), top. When $\beta < 2$ the system undergoes an irreversible collapse. (c) The system recoverability depends on the intersection points of F(x) and $M_2(x)$. Hence we plot F(x) as appears in (3.11) for different values of ω and κ (purple), and $M_2(x) = x^h/(1+x^h)$, for h=1 (yellow). For $\omega = 0.7$ the plot follows the pattern of case 1 - unrecoverable, while for $\omega = 1$ it transitions to case 2 - recoverable. (d) - (e) The same analysis for the case $h \to \infty$. In this limit the activation function $M_2(x)$ behaves as a step function. We find that here the structure of F(x), and hence the recoverability of the system, is independent of κ , affected solely by ω .

3.1 Cellular dynamics

We consider gene-regulatory dynamics, as captured by the Michaelis-Menten model [2, 7], for which (1.1) takes the form

$$\frac{\mathrm{d}x_i}{\mathrm{d}t} = -Bx_i^a + \omega \sum_{j=1}^{N} A_{ij} \frac{x_j^h}{1 + x_j^h}.$$
 (3.1)

Under this framework $M_0(x_i) = -Bx_i^a$, describing degradation (a = 1), dimerization (a = 2) or a more complex bio-chemical depletion process (fractional a), occurring at a rate B [8]. For simplicity, in our simulations we set B = 1. The activation interaction is captured by a Hill function of the form $M_1(x_i) = 1$, $M_2(x_j) = x_j^h/(1 + x_j^h)$, a switch-like function that saturates to $M_2(x_j) \to 1$ for large x_j , representing j's positive, albeit bounded, contribution to i's activity $x_i(t)$.

3.1.1 Free system

First we seek the natural fixed-points of (3.1), by mapping it to the one dimensional space of $\bar{\mathbf{x}}$ via Eq. (1.4). We arrive at

$$\frac{\mathrm{d}\bar{\mathbf{x}}}{\mathrm{d}t} = -\bar{\mathbf{x}}^a + \beta \frac{\bar{\mathbf{x}}^h}{1 + \bar{\mathbf{x}}^h},\tag{3.2}$$

whose fixed-points, obtained by setting $d\bar{\mathbf{x}}/dt = 0$, follow

$$\bar{\mathbf{x}}_0 = 0, \tag{3.3}$$

the inactive state, and

$$\beta = \bar{\mathbf{x}}_{\alpha}^{a} \left(1 + \bar{\mathbf{x}}_{\alpha}^{-h} \right), \tag{3.4}$$

whose solutions provide the potentially active and intermediate states. For a = 1, h = 2, the system we examine in the main text, Eqs. (3.3) and (3.4) provide the three solutions shown in Fig. 3b (see also **Box 1**): an always stable $\bar{\mathbf{x}}_0$ (red), and a stable $\bar{\mathbf{x}}_1$ (green) for $\beta > \beta_c$. The basins of attraction of $\bar{\mathbf{x}}_0$ and $\bar{\mathbf{x}}_1$ are separated by the intermediate unstable state $\bar{\mathbf{x}}_2$ (grey dashed line).

To obtain the critical point β_c we analyze the stability of $\bar{\mathbf{x}}_1$ using condition (1.6). At criticality we replace the inequality by an equality, obtaining

$$-a\bar{\mathbf{x}}^{a-1} + \beta \frac{h\bar{\mathbf{x}}^{h-1}}{(1+\bar{\mathbf{x}}^h)^2} = 0.$$
 (3.5)

Together with Eq. (3.4) we arrive at the solution

$$\bar{\mathbf{x}}_c = \left(\frac{h}{a} - 1\right)^{1/h}$$

$$\beta_c = \frac{h}{a} \left(\frac{h}{a} - 1\right)^{a/h - 1},$$
(3.6)

capturing the bifurcation in Fig. 3b, where the active state (green) emerges as a stable fixed-point at $\beta \geq \beta_c$.

Setting a=1, h=2, the parameters used in the main-text simulations we obtain

$$\bar{\mathbf{x}}_c = 1$$

$$\beta_c = 2,$$
(3.7)

precisely the transitions observed in Fig. 3b. Therefore, the free system exhibits an inactive phase for $\beta < 2$, and a bi-stable regime (grey shaded) for $\beta > 2$, where both $\bar{\mathbf{x}}_0$ and $\bar{\mathbf{x}}_1$ are potentially stable.

3.1.2 Reigniting

To examine the behavior of our cellular dynamics (3.1) under reigniting we seek to construct the recurrence relation (2.32), and specifically the function F(x) in (2.33). First we write

$$R(x) = x^a (3.8)$$

$$R^{-1}(x) = x^{1/a} (3.9)$$

$$M_2(x) = \frac{x^h}{(1+x^h)}, (3.10)$$

where we used (2.22) to obtain R(x). Setting a = 1, we can now collect all the terms to construct F(x), providing us with

$$F(x) = \frac{x}{\omega} - \kappa M_2 \left(\omega M_2(x) \right) = \frac{x}{\omega} - \kappa \frac{1}{1 + \omega^{-h} (1 + x^{-h})^h}$$
 (3.11)

a function whose shape depends on the topological parameters κ and ω . Note that here $\bar{\mathbf{x}}_0 = 0$, and hence $M_2(\bar{\mathbf{x}}_0) = 0$ on the r.h.s. of (2.33). Equation (3.11) maps to F(x) of Eq. (10) in the main text under a = 1. Varying κ and ω we can observe the recoverability of our system as F(x) transitions from case 1 to case 3 of Fig. 2. Two specific examples are presented in Fig. 3b and c. The first with $\kappa = 5$ and $\omega = 0.7$ falls under case 1, and therefore it is unrecoverable, and the second, in which the weight is increased to $\omega = 1$ follows case 3, *i.e.* recoverable.

To obtain the complete phase diagram and hence the boundaries of the recoverable phase, as we do in Fig. 3k - m of the main text, we systematically plot F(x) in (3.11) for a range of κ , ω values, seeking for each κ the critical ω in which F(x) transitions to the form of

case 3. These critical transition points provide the theoretical phase boundaries (Fig. 3k - m, white solid lines). At the same time we tested numerically, for each κ, ω combination whether single-node reigniting indeed reactivates the system (yellow vs. blue shaded areas).

3.1.3 The role of the Hill coefficient

The Hill coefficient h in (3.1) determines the saturation rate of the activation function $M_2(x)$. A small h captures a mild activation, in which $M_2(x)$ increases gradually with x, while $h \to \infty$ describes an effective step-function of the form

$$M_2(x) = \lim_{h \to \infty} \left(\frac{x^h}{1 + x^h} \right) = \theta(x - 1), \tag{3.12}$$

being $M_2(x) = 1$ (activation) if x > 1 and $M_2(x) = 0$ otherwise; $\theta(x)$ is the Heaviside step-function. Taking this limit in (3.11) we obtain

$$\lim_{h \to \infty} F(x) = x/w - \kappa \theta(\omega - 1)\theta(x - 1). \tag{3.13}$$

For $\omega < 1$ we have

$$F(x) = \frac{1}{\omega}x,\tag{3.14}$$

a linear function whose slope is $1/\omega > 1$. This function has a single intersection $M_2(x) = \theta(x-1)$ at x=0, therefore rendering the system unrecoverable (Fig. 3e, left). In case $\omega \ge 1$ Eq. (3.13) becomes

$$F(x) = \frac{1}{\omega}x - \kappa\theta(x-1),\tag{3.15}$$

having two intersections with $M_2(x)$, describing a recoverable system for $\Delta \geq 1$ (Fig. 3e, right).

This describes a limit in which κ plays no role in recoverability, and reigniting is driven solely by ω , as discussed in the main text under Restructuring guidelines.

3.2 Neuronal dynamics

We consider the Cowan-Wilson model [9, 10] for excitation in neuronal networks, writing

$$\frac{\mathrm{d}x_i}{\mathrm{d}t} = -x_i + \omega \sum_{j=1}^{N} A_{ij} \frac{1}{1 + e^{\mu - \delta x_j}},$$
(3.16)

which we examine under $\mu = 5$ and $\delta = 1$.

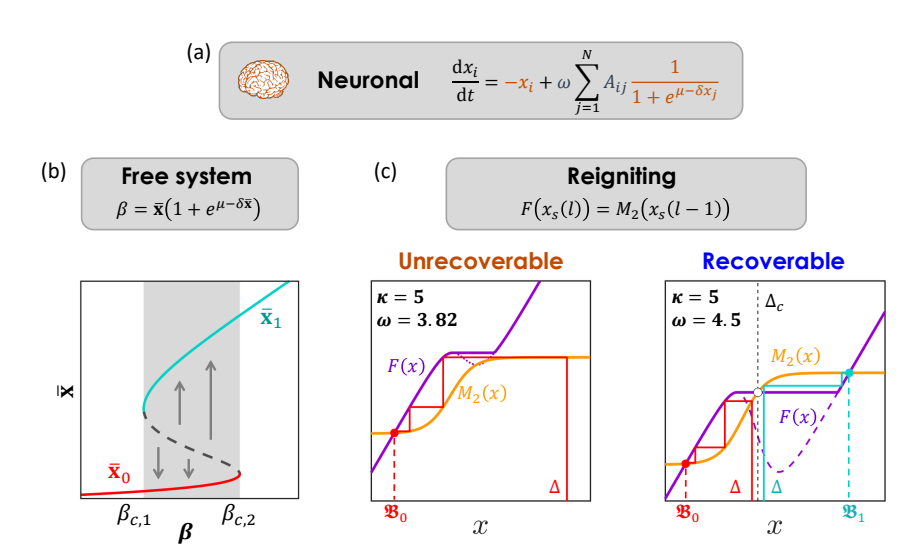


Figure 4: **Neuronal dynamics**. (a) The Cowan-Wilson model. (b) \bar{x} vs. β as obtained from Eq. (3.18) with $\mu = 5, \delta = 1$. The system exhibits two potential states $\bar{\mathbf{x}}_0$ (red) and $\bar{\mathbf{x}}_1$ (green), separated by a bi-stable phase (grey shaded). (c) F(x) (purple) from (3.22) and $M_2(x)$ (yellow) from (3.21) for an unrecoverable system ($\omega = 3.82$, left) and a recoverable one ($\omega = 4.5$, right).

3.2.1 Free system

To obtain the fixed-points of the system we use the mapping of (1.4) to reduce (3.16) into

$$\frac{\mathrm{d}\bar{\mathbf{x}}}{\mathrm{d}t} = -\bar{\mathbf{x}} + \beta \frac{1}{1 + e^{\mu - \delta\bar{\mathbf{x}}}},\tag{3.17}$$

whose fixed-points follow

$$\beta = \bar{\mathbf{x}}_{\alpha} (1 + e^{\mu - \delta \bar{\mathbf{x}}_{\alpha}}). \tag{3.18}$$

Plotting $\bar{\mathbf{x}}$ vs. β (Fig. 4b) we obtain the dynamic phases of the system - the *inactive* state \mathbf{x}_0 (red), in which all activities are suppressed, is obtained when the network is extremely sparse, *i.e.* small β ; the *active* \mathbf{x}_1 (green), in which x_i are relatively high, is observed when β is large. In between these two extremes the system features a *bi-stable* phase, in which both \mathbf{x}_0 and \mathbf{x}_1 are potentially stable. These phases are separated by two critical points $\beta_{c,1} < \beta_{c,2}$, predicting a hysteresis phenomenon: if β was driven below $\beta_{c,1}$ and the system has failed, it will not spontaneously recover unless we retrieve β to be above $\beta_{c,2}$. Hence, we seek the sub-space within the bi stable regime, $\beta_{c,1} < \beta < \beta_{c,2}$, in which the system can reignited.

3.2.2 Reigniting

The relevant functions to construct F(x) (2.33) are

$$R(x) = x, (3.19)$$

$$R^{-1}(x) = x, (3.20)$$

$$M_2(x) = \frac{1}{(1 + e^{\mu - \delta x})},$$
 (3.21)

from which we obtain

$$F(x) = \frac{x}{\omega} - \kappa M_2 \left(\omega M_2(x) + \omega \kappa M_2(\bar{\mathbf{x}}_0) \right). \tag{3.22}$$

Once again we arrive at a function which depends on κ and ω , sometimes following the unrecoverable case 1 (Fig. 4c, left), and sometimes following the recoverable case 3 (Fig. 4c, right).

3.3 Mutualistic population dynamics

We examine symbiotic interactions in ecological networks, such as plant-pollinator relationships captured by

$$\frac{\mathrm{d}x_i}{\mathrm{d}t} = F + Bx_i \left(1 - \frac{x_i}{C}\right) (x_i - K) + \omega \sum_{j=1}^N A_{ij} x_i x_j. \tag{3.23}$$

The self dynamics describes migration at a rate F coupled with logistic growth at rate B, with the system carrying capacity set to C, and the Alley effect with strength K. The mutualistic interaction follows the Lotka-Volterra form $x_i x_j$. In our simulations we set F = 5, B = 0.9, C = 3 and K = 10.

3.3.1 Free system

Using Eq. (1.4) we write

$$\frac{\mathrm{d}\bar{\mathbf{x}}}{\mathrm{d}t} = F + B\bar{\mathbf{x}}\left(1 - \frac{\bar{\mathbf{x}}}{C}\right)(\bar{\mathbf{x}} - K) + \beta\bar{\mathbf{x}}^2,\tag{3.24}$$

obtaining the fixed-points from

$$\beta = \frac{-FC + B\bar{\mathbf{x}}(\bar{\mathbf{x}} - C)(\bar{\mathbf{x}} - K)}{C\bar{\mathbf{x}}^2}.$$
(3.25)

In Fig. 5b we plot $\bar{\mathbf{x}}$ vs. β as obtained from Eq. (3.25) finding two phases. For $\beta < \beta_c$ we observe two fixed-points, $\bar{\mathbf{x}}_0$ (red) and $\bar{\mathbf{x}}_1$ (green), a bi-stable phase, and for $\beta \geq \beta_c$ a single active state $\bar{\mathbf{x}}_1$.

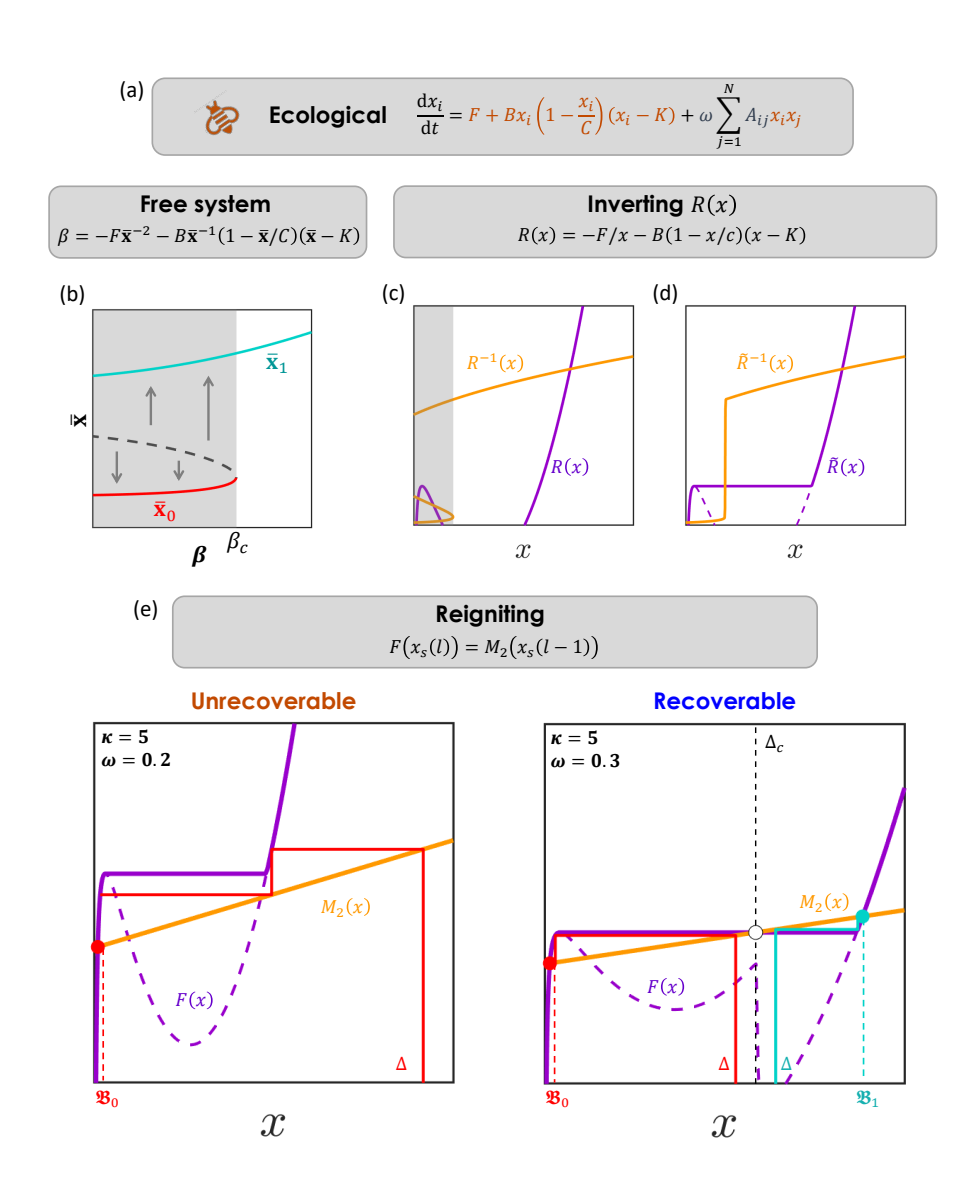


Figure 5: **Ecological dynamics**. (a) Our mutualistic population dynamics model. (b) \bar{x} vs. β as obtained from Eq. (3.25). The system features a bi-stable phase (grey shaded), then at $\beta \geq \beta_c$ transitions to a single active fixed-point. (c) R(x) vs. x (purple) as obtained from (3.27). The function is non-monotonic and hence $R^{-1}(x)$ (yellow) is ill-defined. The dual range in which $R^{-1}(x)$ admits ambiguous solutions (grey shaded) is directly related to the bi-stable phase of the system via Eq. (3.29). The relevant branch is only the lower one, associated with the failed state of the system, on which we employ our reigniting. (d) We preserve only the lower branch by replacing the original R(x) (purple dashed line) with a monotonous $\tilde{R}(x)$, in which we introduce a plateau instead of the non-monotonic range (purple solid line). The resulting function can now be unambiguously inverted (yellow). (e) F(x) (purple) from (3.30) and $M_2(x)$ (yellow) from (3.26) for an unrecoverable system ($\omega = 0.2$, left) and a recoverable one ($\omega = 0.3$, right).

3.3.2 Reigniting

Here the functions comprising F(x) in (2.33) are

$$M_2(x) = x, (3.26)$$

and

$$R(x) = -\frac{F}{x} - B\left(1 - \frac{x}{C}\right)(x - K). \tag{3.27}$$

The challenge is that in order to construct F(x) we must invert R(x), which as indicated in Fig. 5c is non-monotonic and hence, in principle, non-invertible. The result is that $R^{-1}(x)$ is ill-defined for a certain range of x, matching potentially two values for the same x. This ambiguity is directly related to the bi-stability of \bar{x}_0 and $\bar{\mathbf{x}}_1$ in the range $\beta < \beta_c$. Indeed, Eq. (3.25) can be written in the form

$$\beta \bar{\mathbf{x}} = R(\bar{\mathbf{x}}),\tag{3.28}$$

from which is follows that

$$\bar{\mathbf{x}} = R^{-1}(\beta \bar{\mathbf{x}}),\tag{3.29}$$

in which the ambiguous value of $R^{-1}(\beta \bar{\mathbf{x}})$ for $\beta < \beta_c$ is precisely to root of the observed bi-stability. It, therefore, follows that of the two branches in $R^{-1}(x)$ the relevant branch is the one associated with $\bar{\mathbf{x}}_0$, as, indeed, the reigniting is applied on the failed state. Hence, to correct for this ambiguity we use a similar construction to the one shown in Fig. 2d when treating the non-monotonic F(x), namely, we eliminate the non-monotonic range of the function by replacing it with a constant plateau. This leads to the corrected $\tilde{R}(x)$ shown in Fig. 5d, in which the original function (dashed-line) is replaced by a corrected monotonic $\tilde{R}(x)$ (solid line). Its inverse $\tilde{R}^{-1}(x)$ is now well-defined, and, most importantly, suitable to predict the system's response to reigniting from a failed initial condition. We can now use this corrected function to construct F(x) in (2.33) providing

$$F(x) = \frac{\tilde{R}(x)}{\omega} - \kappa \tilde{R}^{-1} \Big(\omega x + \omega \kappa \bar{\mathbf{x}}_0 \Big). \tag{3.30}$$

We can now systematically use our cobweb plots to assess the system recoverability for different combinations of ω and κ (Fig. 5e).

4 Numerical analysis

4.1 Numerical integration

To numerically test our predictions we constructed Eq. (1.1) for each of the systems in Sec. 3, using the appropriate A_{ij} (Scale-free, Erdős-Rényi, empirical, etc.). We then used a second-order Runge-Kutta stepper (Matlab's ode23) to numerically solve the resulting equations. Starting from a pre-selected initial condition $x_i(t=0)$, $i=1,\ldots,N$ we allowed the system to reach steady-state by waiting for $\dot{x}_i \to 0$. To numerically realize this limit we implemented the termination condition

$$\max_{i=1}^{N} \left| \frac{x_i(t_n) - x_i(t_{n-1})}{\Delta t_n} \right| < \varepsilon, \tag{4.1}$$

where t_n is the time stamp of the *n*th Runge-Kutta step and $\Delta t_n = t_n - t_{n-1}$. As the system approaches a steady-state, the activities $x_i(t_n)$ become almost independent of time, and the numerical derivative $\dot{x}_i = (x_i(t_n) - x_i(t_{n-1}))/\Delta t_n$ becomes small. The condition (4.1) guarantees that the maximum of \dot{x}_i over all activities $x_i(t_n)$ is smaller than the pre-defined termination variable ε . In our simulations, across the different dynamics we tested, we set $\varepsilon \leq 10^{-2}$ to ensure that our system is sufficiently close to the *true* steady-state.

In case of bi-stability we examined the convergence of the system from multiple initial conditions. For example, setting $\mathbf{x}(t=0)$ to a low value in \mathfrak{B}_0 ensures convergence to \mathbf{x}_0 , in case \mathbf{x}_0 is stable; setting it in \mathfrak{B}_1 ensures convergence to \mathbf{x}_1 , in case \mathbf{x}_1 is also stable. If only one of the states is stable - all initial conditions will converge to that single fixed-point.

4.2 Reigniting

To simulate reigniting we set the system at the initial condition to $\mathbf{x}(t=0) = \mathbf{x}_0$. We then select a random node s, decouple it from the remaining N equations and set its state to $x_s(t) = \Delta$. Together with the remaining N-1 equations of (1.1) we arrive at Eq. (2.1), which takes the form

$$\begin{cases} x_s(t) = \Delta \\ \frac{\mathrm{d}x_i}{\mathrm{d}t} = M_0(x_i) + \omega \sum_{j=1}^N A_{ij} M_1(x_i) M_2(x_j) & i \neq s \end{cases}$$
(4.2)

Integrating this equation until reaching steady-state, *i.e.* condition (4.1), we find the final state $\mathbf{x}_{\text{Forced}}$ of the *forced* system. We then relax our forcing, re-couple $x_s(t)$ to the remaining N-1 equations, and allow the system to reach its final state. This is achieved by setting the new initial condition to $\mathbf{x}(t=0) = \mathbf{x}_{\text{Forced}}$, and numerically solving Eq. (1.1) until reaching steady-state. In case $\mathbf{x}_{\text{Forced}} \in \mathfrak{B}_1$, a successful reigniting, the system will reach \mathbf{x}_1 . If, however, our reigniting failed, and $\mathbf{x}_{\text{Forced}}$ remains in \mathfrak{B}_0 , the system, after forcing ceases, will revert to the undesired \mathbf{x}_0 .

4.3 Constructing the phase diagrams in Figs. 3-5

We used the Erdős-Rényi random network model with different connection probabilities p to construct a set of 150 networks with $N=10^4$ nodes each, spanning a range of residual degrees κ , as detailed in Table 1. Together, for each system we examined 15 different values of κ , with 10 independent realizations for each value. For example, in our Cellular dynamic we first set $p=3\times 10^{-4}$, which, on average, for an Erdős-Rényi random network, provides $\kappa\approx 3$. We then constructed 10 such networks, to gain several realizations of the same random graph. Repeating the process for higher p values we arrive at 10×15 networks, comprising 10 realizations of 15 different κ values.

Next, we matched each of these networks with different weights ω whose range is shown in Table 1. These ranges of κ , ω is selected in each system to best portray the different phases. Gradually increasing ω for each of the 150 networks we observed the critical transition points between active, inactive, bi-stable, recoverable and non-recoverable states. Together this process examined a repository of thousands of different networks with varying κ and ω . For each of these networks we obtained the steady-state/s as explained in Sec. 4.1, observing whether they are in the active, inactive or bi-stable regime. We then also tested whether they are recoverable via single-node reigniting, following Sec. 4.2. As explained each data point (κ, ω) in the resulting phase-diagrams is obtained from averaging over 10 independent realizations. In each realization we selected randomly the source node for reigniting.

4.4 Model and empirical networks

We used model and real networks, as summarized below:

ER. Erdős-Rényi random networks with $N=10^4$ nodes and varying connection probability p, to inspect the range of κ values. The phase diagrams were formed using this set of model networks.

PPI Yeast (Regulatory). The yeast protein-protein interaction network, an empirical scale-free consisting of 1,647 nodes (proteins) and 5,036 undirected links, representing chemical interactions between proteins [11].

PPI Human (Regulatory). The human protein-protein interaction network, a scale-free network, consisting of N=2,035 nodes (protein) and L=13,806 protein-protein interaction links [12].

Brain (Neuronal). Mapping the physical fiber bundle connections between 998 brain regions, as measured using diffusion tensor imaging techniques [13]. The empirical network is relatively dense, having $\kappa=41.91$, rendering naturally deep in the right hand side of the phase diagram (Fig. 4d, main text). In this limit the recoverable phase is practically unobservable, as the system transitions directly from the unrecoverable phase (yellow) to the spontaneously active phase (green). Therefore, to observe the recoverability, we examined reigniting on a perturbed Brain network in which we randomly deleted 83.9% of the links, bringing our network to $\kappa=6.61$. Under these conditions we can construct two networks one unrecoverable with small ω (Fig. 4d, orange dot), and the other recoverable with larger

	System	Model	Parameters	Networks	κ Range	ω Range
1	Cellular	$\frac{\mathrm{d}x_l}{\mathrm{d}t} = -Bx_l^a + \omega \sum_{j=1}^N A_{ij} \frac{x_j^h}{1 + x_j^h}$	B = 1 $a = 1$ $h = 2$	ER PPI Yeast PPI Human	$3 < \kappa < 30$	$0.03 < \omega < 5$
	Neuronal	$\frac{\mathrm{d}x_l}{\mathrm{d}t} = -x_l + \omega \sum_{j=1}^N A_{lj} \frac{1}{1 + e^{\mu - \delta x_j}}$	$\mu = 5$ $\delta = 1$	ER Brain	$3 < \kappa < 25$	$0 < \omega < 8$
B	Ecological	$\frac{\mathrm{d}x_i}{\mathrm{d}t} = F + Bx_i \left(1 - \frac{x_i}{C}\right)(x_i - K) + \omega \sum_{j=1}^{N} A_{ij}x_ix_j$	F = 5 $B = 0.9$ $C = 3$ $K = 10$	ER Eco	$4 < \kappa < 40$	$0.09 < \omega < 2$

Table 1: Summary of models and parameters. For each system we show the relevant dynamic equation (Model), and the parameters we used in our simulations. Each system was examined on a set of relevant networks. When construction the phase-diagrams of Fig. 3 - 5 of the main text, we use Erdős-Rényi networks with a range of κ and ω values, as shown in the two rightmost columns.

 ω (Fig. 4d, light blue dot).

ECO (Ecological). To construct the mutualistic ecological networks we collected data on symbiotic interactions of plants and pollinators in Carlinville Illinois from [14]. The resulting $456 \times 1,429$ network M_{nm} is a bipartite graph linking the 456 plants $(n=1,\ldots,456)$ with their 1,429 pollinators $(m=1,\ldots,1,429)$. When a pair of plants is visited by the same pollinator they mutually benefit each other indirectly, by increasing the pollinator population. Similarly pollinators sharing the same plants also share an indirect mutualistic interaction. Hence we can collapse M_{ik} to construct either the pollinator of the plant network. Here we used the larger $1,429 \times 1,429$ pollinator network

$$A_{ij} = \begin{cases} 1 & \text{if } \max_{k=1}^{456} \left(M_{ki} M_{kj} \right) > 0 \\ 0 & \text{if } \max_{k=1}^{456} \left(M_{ki} M_{kj} \right) = 0, \end{cases}$$

$$(4.3)$$

which prescribes a link $(A_{ij} = 1)$ between pollinators i and j if they share at least one mutual plant. This process potentially allows us to have isolated components, e.g., single disconnected nodes. The state of these isolated nodes is decoupled from the state of the rest of the network, and hence in our analysis we only focused on the giant connected component of A_{ij} , comprising only 1,044 pollinators, eliminating 385 isolated pollinators in A_{ij} . Similarly to the Brain networks, also here we examine reigniting on a sparse network, in which we removed 50.11% of the links, setting κ to 11.13, in the area that allows us to examine the window of recoverability (Fig. 4i, main text).

References

- [1] J. Gao, B. Barzel and A.-L. Barabási. Universal resilience patterns in complex networks. *Nature*, 530:307—-312, 2016.
- [2] U. Alon. An Introduction to Systems Biology: Design Principles of Biological Circuits. Chapman & Hall, London, U.K., 2006.
- [3] B. Barzel and A.-L. Barabási. Network link prediction by global silencing of indirect correlations. *Nature Biotechnology*, 31:720 725, 2013.
- [4] M.E.J. Newman. Networks an introduction. Oxford University Press, New York, 2010.
- [5] R.M. May. Simple mathematical models with very complicated dynamics. *Nature*, 261:459–467, 1976.
- [6] S.H. Strogatz. Nonlinear dynamics and chaos with student solutions manual: With applications to physics, biology, chemistry, and engineering. CRC press, 2018.
- [7] G. Karlebach and R. Shamir. Modelling and analysis of gene regulatory networks. *Nature Reviews*, 9:770–780, 2008.
- [8] B. Barzel and O. Biham. Binomial moment equations for stochastic reaction systems. *Physical Review Letters*, 106:150602–5, 2011.
- [9] H.R. Wilson and J.D. Cowan. Excitatory and inhibitory interactions in localized populations of model neurons. *Biophysical Journal*, 12(1):1–24, 1972.
- [10] H.R. Wilson and J.D. Cowan. A mathematical theory of the functional dynamics of cortical and thalamic nervous tissue. *Kybernetik*, 13(2):55–80, 1973.
- [11] H. Yu et al. High-quality binary protein interaction map of the yeast interactome network. Science, 322:104–110, 2008.
- [12] J.F. Rual *et al.* Towards a proteome-scale map of the human protein-protein interaction network. *Nature*, 437:1173–1178, 2005.
- [13] E. Bullmore and O. Sporns. Complex brain networks: graph theoretical analysis of structural and functional systems. *Nature reviews neuroscience*, 10(3):186–198, 2009.
- [14] Interaction web database. http://www.nceas.ucsb.edu/interactionweb/resources.